Molecular basis for the interaction of Mint proteins with Munc18-1 and interactome analyses with AlphaFold2

Saroja Weeratunga[1], Rachel S. Gormal[2], Emma K. Livingstone[1], Frederic A. Meunier[2,3] and Brett M. Collins[1]*

[1]The University of Queensland, Institute for Molecular Bioscience, Queensland, 4072, Australia; [2]Clem Jones Centre for Ageing and Dementia Research, Queensland Brain Institute, The University of Queensland, Queensland, 4072, Australia; [3]The University of Queensland, School of Biomedical Sciences, Queensland, 4072, Australia;

Running Title: Interaction of Mints with Munc18-1

*Corresponding author:
Brett Collins, +61 (0)7 33462043, Email: b.collins@imb.uq.edu.au

Keywords – ARF3, AP3, neurexin, CASK, KCNJ, HXC9, USP22, calsyntenin, LRP, TJAP1, Munc18, Mint, X11, AlphaFold, SNARE, STXBP1, APP.

SUMMARY

Munc18-interacting proteins (Mints) are multi-domain adaptors that regulate neuronal membrane trafficking, signalling and neurotransmission. Mint1 and Mint2 are highly expressed in the brain and play overlapping roles in the regulation of synaptic vesicle fusion required for neurotransmitter release by interacting with the essential synaptic protein Munc18-1. The mechanism by which Mint1 mediates the interaction of Munc18-1 with Syntaxin1a (Sx1a) to control formation of the fusogenic SNARE complex and facilitate neurotransmission remains unclear. Here, we have studied both the specific interactions of the neuronal Mint proteins with Munc18-1 as well as their wider interactome. Using biochemical and biophysical binding approaches we identify a short acidic α-helical motif (AHM) within Mint1 and Mint2 that is necessary and sufficient for specific binding to Munc18-1. *In silico* modelling of this interaction with AlphaFold2 and extensive validation by structure-based mutagenesis *in vitro*, showed that the AHM in Mint forms an α-helical structure, binds a conserved surface on Munc18-1 domain3b. Although Munc18-1 can interact with Mint and Sx1a proteins simultaneously we find they have mutually reduced affinities, suggesting an allosteric coupling between the two proteins. Finally, using AlphaFold2 we probed the wider network of interactions governed by the Mint scaffolds, and provide a structural model for their assembly with a variety of known and novel regulatory and cargo proteins including ARF3/ARF4 small GTPases, neurexins, and the AP3 clathrin adaptor complex. Overall, our data provides insights into the diversity of interactions mediated by the Mint family and suggests that Mints may help to control a key trigger point in SNARE complex assembly and vesicle fusion.

INTRODUCTION

Synaptic vesicle fusion and release of neurotransmitters requires the formation of specific complexes between vesicular and plasma membrane SNARE proteins (soluble *N*-ethylmaleimide-sensitive factor attachment receptors). The vesicular v-SNAREs and target t-SNAREs form an α-helical coiled-coil assembly that provides the necessary energy to bring the two opposing lipid membranes together for membrane fusion. Munc18-1 (also called Munc18a, syntaxin-binding protein 1 (STXBP1), and neuronal Sec1 (nSec1)) is a member of the Sec1/Munc18 (SM) protein family, and an essential regulatory protein required for the assembly of this SNARE complex in neuronal membrane fusion. Munc18-1 binds with high affinity to the target or Qa-SNARE Syntaxin1a (Sx1a) and mediates both its trafficking and its incorporation into the SNARE complex with the Qbc-SNARE SNAP25 and the vesicle or R-SNARE Vamp2.

Importantly, Munc18-1 also interacts with other regulatory proteins including Munc13 and the two Munc-interacting protein (Mint) paralogues Mint1 and Mint2. Mints (also known as X11, amyloid precursor protein-binding family A (APBA) or Lin-10 proteins) are multi domain scaffolds that participate in a host of protein-protein interactions. The human genome encodes three Mint homologues, Mint1, Mint2 and Mint3 (Rogelj et al., 2006) (**Fig. 1A**). Mint1 and Mint2 are highly enriched in brain and spinal cord tissue, while Mint3 is ubiquitously expressed (Biederer et al., 2002; Ho et al., 2002b; Lee et al., 2003; Motodate et al., 2016; Tomita et al., 1999). Structurally, Mint proteins are composed of similar C-terminal phosphotyrosine binding (PTB) and tandem PSD95/Dlg/ZO-1 (PDZ) domains, and possess highly extended intrinsically disordered N-terminal domains that mediate paralogue-specific interactions. As scaffold proteins, the PTB domains of the Mint proteins interact with various ligands containing NPxY sequences (x is any amino acid) such as the amyloid precursor protein (APP), APP-like proteins APLP1 and APLP2, and TrkA (Borg et al., 1996; Borg et al., 1998; Caster and Kahn, 2013; Chaufty et al., 2012; Ho et al., 2008; Matos et al., 2012; Saito et al., 2011; Sakuma et al., 2009; Sullivan et al., 2014; Tomita *et al.*, 1999; Xie et al., 2013; Zhang et al., 2009; Zhang et al., 1997), while the PDZ domains of the Mint proteins bind to C-terminal PDZ binding motifs (PDZbms) in molecules including NMDA receptors, kalirin-7, neurexins, ApoER2 and LDLR (Biederer and Sudhof, 2000; Gotthardt et al., 2000; Jones et al., 2014; Minami et al., 2010; Motodate et al., 2019). The N-terminus of the Mint proteins contains both conserved and divergent sequences that mediate distinct protein-protein interactions. An N-terminal sequence specific to Mint1 called the CASK-interacting domain (CID) binds specifically to Ca^{2+}/calmodulin-dependent serine protein kinase (CASK/Lin-2) (a multi domain adapter and kinase) forming a tripartite complex with Veli/Lin-7 family proteins and neurexins at the pre-synapse (Borg *et al.*, 1998; Stafford et al., 2011; Tabuchi et al., 2002; Wu et al., 2020; Zhang et al., 2020). In contrast, the N-terminal regions of both neuronally expressed Mint1 and Mint2 proteins specifically interact with Munc18-1 via a sequence termed the Munc18-1-interacting domain (MID) (Biederer and Sudhof, 2000; Graham et al., 2011; Han et al., 2014; Ho *et al.*, 2002b; Okamoto and Sudhof, 1997; 1998; Park et al., 2012). However the mechanism of Munc18-1 interaction is unknown.

The importance of Mint1 in neuronal function is apparent in studies showing, homozygous deletions of Mint1 or Mint2 display disrupted GABAergic transmission (Ho et al., 2003; Sano et al., 2006), however knockout of both Mint1 and Mint2 neuronal isoforms leads to lethality at birth in most animals, with surviving mice displaying deficits in motor behaviours and spontaneous neurotransmitter release. A prominent phenotype of knockout animals is an alteration in APP trafficking and processing to the Alzheimer's plaque peptide amyloid β (Aβ) (Gross et al., 2013; Sullivan *et al.*, 2014), although the changes appear to be dependent on specific knockout conditions with both an increase (Kondo et al., 2010; Saluja et al., 2009; Sano *et al.*, 2006) and decrease (Ho *et al.*, 2008; Sullivan *et al.*, 2014) in Aβ production reported. Thus, the molecular interactions between Mints, synaptic proteins and trafficking partners involved in neurodegenerative diseases is of broad interest to the field.

Mutations in the core neuronal pre-synaptic machinery including Munc18-1 and Sx1a lead to a distinct but overlapping set of neurodevelopmental disorders, with symptoms including neurodevelopmental delay, intellectual disability and early infantile epileptic encephalopathy (Lanoue et al., 2019; Verhage and Sorensen, 2020). Mutations in the Mint1-assocated CASK protein have also been found to cause neurodevelopmental disorders with similar features, including mental retardation and microcephaly with ophthalmic atrophy (Hayashi et al., 2017; Hsueh, 2009; LaConte et al., 2019; Piluso et al., 2009), and the human disease linked missense variant p.Leu209Pro in CASK variant linked to optic nerve hypoplasia specifically disrupts Mint1 binding without impacting other protein interactions (LaConte *et al.*, 2019). Mutations in the Mint proteins themselves have not yet been specifically linked to similar disorders, although copy number variations in Mint2 have been described in patients with epilepsy and intellectual disability (Peycheva et al., 2018). In addition, variants in Mint2 have been linked to autism spectrum disorder, potentially through disruption of neurexin trafficking (Babatz et al., 2009; Lin et al., 2019). By assessing the mechanisms responsible for Mint1 binding to a range of protein partners, we aim to provide a framework that can contribute to the understanding of how Mint1 might modulate a role during neurotransmission and trafficking.

In this work we examined the mechanism of binding between the Mint MID domain Munc18-1. Using truncations and peptide mutagenesis have defined a minimal acidic short linear interaction motif (SLiM) of thirteen amino acids in Mint1 and Mint2 that is required and sufficient for Munc18-1 interaction. Although phosphorylation in this region of Mint1 can regulate binding to other proteins such as APP, this does not appear to influence Munc18-1 affinity. Using AlphaFold2 we generated a model of the Mint1 sequence bound to Munc18-1 which shows that the peptide forms an α-helical structure bound to Munc18-1 at an entirely novel binding site in domain 3b. The binding of this acidic-helical motif (AHM) was extensively validated by mutations in key Mint1 and Munc18-1 residues that disrupt their interaction. Notably the AlphaFold2 model and crystal structure match precisely in all key details. Although the respective Mint1/2 and Sx1a binding sites in domain 3b and domains 1/3a are distinct from each other, their individual Munc18-1 binding affinities are reduced in the presence of the other ligand. We speculate that this antagonistic allosteric interaction between the two proteins

may be important for regulating Munc18-1 templating of SNARE-complex formation. Finally, building on the successful structural predictions of Mint1 with AlphaFold2, we have explored the wider network of interactions mediated by the Mint scaffolds and provide an overall model for its assembly with both effector and regulatory proteins, including the identification of novel binding sites in the Mint PDZ domains for ARF small GTPases and in the Mint PTB domains with non-canonical peptide sequences.

RESULTS

Mapping the Munc18-1-binding sequence of Mint1 and Mint2

A number of studies have shown that both Mint1 and Mint2 homologues can interact with Munc18-1, using methods including immunoprecipitation and yeast two-hybrid assays (Biederer and Sudhof, 2000; Ho et al., 2002a; Lee et al., 2004; M. Okamoto, 1997; Okamoto and Sudhof, 1997). Mint proteins are multi-domain scaffolds with a C-terminal PTB domain and tandem PDZ domains preceded by a long and unfolded N-terminal sequence that shows low sequence homology across the family (**Fig. 1A; Fig. S1**). Munc18-1 binding has been mapped by yeast two-hybrid assays to a region termed the 'Munc18-interacting domain' (MID) within the N-terminus of the neuronal Mint1 and Mint2 proteins consisting of residues 226-314 and 185-270 respectively (Okamoto and Sudhof, 1997). We first confirmed the direct interaction of Mint1 with purified Munc18-1, performing a GST pull-down assay using the human Mint1 MID as bait (residues 222-314). This showed clear binding between the two proteins that was specific for the neuronal Munc18-1 protein as we did not detect any interaction with Munc18-3 (**Fig. 1B**). As the entire N-terminus of Mint1 including the MID is expected to be unstructured in isolation, we hypothesised that Munc18-1 may be binding to a shorter peptide sequence or SLiM (Diella et al., 2008) within the MID. To test this, we generated several truncated Mint1 MID sequences and tested their binding to Munc18-1 by GST pull-down assay (**Fig. 1C**). This showed that a twenty-one amino acid region encompassing residues 261-282 was required and sufficient for Munc18-1 binding.

The binding of a synthetic Mint1 peptide to Munc18-1 was next measured by isothermal titration calorimetry (ITC) and the affinity (K_d) of the interaction was found to be 12.1 ± 1.8 μM (**Fig. 2A, Fig. 2B; Table 1**). With a direct assay for Mint1(261-282) peptide interaction we generated a series of N and C-terminal deletions and found that the minimal binding sequence for Munc18-1 in human Mint1 consists of the thirteen residues from Glu267 to Ser280 (**Fig. 2B**; **Table 1; Fig. S2**). This region is notably the most highly conserved sequence in the N-terminus of Mint1 and Mint2 across species (**Fig. S1**). In line with this we also find that an overlapping peptide from human Mint2 shares a similar binding affinity for Munc18-1 (**Fig. 2B**; **Table 1; Fig. S2**). Within this region the sequence ^{267}EEDIDQIVAE^{276} is invariant across Mint1 and Mint2 homologues from human, fish and xenopus species (although it is not present in worms and flies) (**Fig. S1**), and a series of double alanine substitutions in this sequence showed that all of these residues are important for Munc18-1 interaction by ITC (**Fig. 2B**; **Table 1; Fig. S2**). The conservation of this minimal binding sequence suggests that Munc18-1 interaction with Mint1 or Mint2 plays a critical role in the functions of these proteins.

We confirmed the binding of Mint1 to Munc18-1 in PC12 cells by co-immunoprecipitation. GFP-Mint1 or GFP-Mint1(D269A/I270A) were expressed in PC12 cells and bound to GFP-nanotrap beads followed by blotting for the presence of Munc18-1 (**Fig. 2C**). The mutation D269A/I270A reduced Munc18-1 binding in agreement with our *in vitro* ITC data.

142 ***Phosphomimetic Mint1 mutations do not affect the binding to Munc18***

143 The N-terminal region of Mint1 and Mint2 is predicted to be unstructured and can be phosphorylated
144 at numerous sites as catalogued in the PhosphoSitePlus database (Hornbeck et al., 2015) (**Fig.**
145 **S3A**). There are several potential sites of Ser/Thr phosphorylation adjacent to the minimal Munc18-
146 1 binding sequences of Mint1 and Mint2 (**Fig. S3B**). Given the overall negative electrostatic charge
147 distribution of the Mint1 and Mint2 N-terminal domains (**Fig. S3C**), we speculated that adding further
148 negative charges in the form of phosphorylation might influence the affinity of the Munc18-1
149 interaction. We designed two longer peptides of Mint1 and Mint2 with putative phosphorylated
150 residues altered to phosphomimetic glutamates and tested their binding by ITC (**Fig. 2B**; **Table 1;**
151 **Fig. S2**). Our results suggest that phosphorylation of Mint proteins near to the Munc18-interacting
152 sequence does not play a direct role in modulating the Munc18-1 binding affinity at least *in vitro*.
153 Previous studies showed that Mint1 and Mint2 N-terminal domains can be phosphorylated upstream
154 of the Munc18-1-interacting sequence by the tyrosine kinase c-Src (Dunning et al., 2016). While this
155 enhanced the trafficking of APP via binding the PTB domain, presumably by affecting the overall
156 conformation of Mint1 in some way, it had no effect on Munc18-1 interaction. Phosphorylation of
157 Ser236 and Ser238 in Mint2 also enhance the APP interaction (Sakuma *et al.*, 2009). These sites
158 lie directly adjacent to the Munc18-1-interacting sequence, and our ITC experiments indicate they
159 do not affect Munc18-1 binding (**Fig. 2B**; **Table 1; Fig. S2**). Therefore, it appears that while
160 phosphorylation-dependent conformational changes in the Mint1 N-terminal region play a role in the
161 interactions with APP (and likely other PTB domain-binding transmembrane proteins such as APLP1,
162 APLP2, Megalin and LRP) they are dispensable for Munc18-1 association *in vitro*.

163

164 ***Mint1 forms an acidic α-helical motif that binds to Munc18-1 domain 3b***

165 Despite attempts to crystallise Munc18-1 in complex with various Mint1 peptides we were unable
166 determine a high-resolution structure of this complex, including with stabilized Munc18-1 variants
167 (Peleg et al., 2021). The machine-learning structure-prediction algorithm AlphaFold2 (Evans et al.,
168 2022; Jumper et al., 2021) has been successfully used to predict structures of protein-peptide
169 complexes by ourselves and others (Ko and Lee, 2021; Poetz et al., 2021; Simonetti et al., 2021;
170 Tsaban et al., 2021). We performed a series of modelling experiments to map the complex between
171 Munc18-1 and Mint1 using the ColabFold implementation of AlphaFold2 (Mirdita et al., 2022). We
172 initially predicted the complex between the Mint1 and Munc18-1 full-length proteins (**Fig. S4A**).
173 Across multiple models we assessed (i) the prediction confidence measures (pLDDT and interfacial
174 pTM scores), (ii) the plots of the predicted alignment errors (PAE) and (iii) backbone alignments of
175 the final structures. This identified a high-confidence binding sequence in the N-terminal region of
176 Mint1 that correlated precisely with the binding motif identified in our biochemical experiments (**Fig.**
177 **S4A**).

178 Based on this initial model and our biochemical mapping of the minimal Mint1 sequence for
179 Munc18-1 binding we performed multiple independent predictions using a shorter peptide region,

combined with AMBER energy minimization to optimize amino acid stereochemistry. We consistently found that the minimal sequence of Mint1 was predicted to form an extended α-helical structure that associated with the Munc18-1 domain 3b (**Fig. 3A; Fig. 3B**). This novel binding site is highly conserved in Munc18-1 to a similar degree to the binding site for the Sx1a SNARE protein (**Fig. 3C**). In addition, we found that both the zebrafish Munc18-1 and Mint1 orthologues, and the human Munc18-1 and Mint2 proteins were consistently predicted to form essentially identical structures (**Fig. S4B, S4C**). In contrast, the human Munc18-3 protein was not predicted to form a stable complex with Mint1 (**Fig. S4D**) consistent with their lack of interaction *in vitro* (**Fig. 1B**). Finally, we modelled the tripartite interaction of human Munc18-1 and CASK with an extended Mint1 sequence containing both the Munc18 and CASK-interacting domain (CID) (**Fig. S4E**). The two Mint1 regions were modelled by AlphaFold2 to bind their respective partners in the expected conformations, with the CASK-binding sequence matching closely in structure to the previous crystal structures of the CASK-Mint complex (Wu *et al.*, 2020; Zhang *et al.*, 2020).

The Mint1 interacting sequence forms what we refer to as an acidic α-helical motif (AHM) as proposed by Li and colleagues (Li et al., 2023) (see below), and makes a number of critical contacts with Munc18-1 domain3b including both hydrophobic and electrostatic interactions between conserved sidechains (**Fig. 3D; Movie S1**). Consistent with our truncation and mutation analyses of the Mint1 MID peptides (**Fig. 2B**), all predicted core contacts with Munc18-1 are mediated by Mint1 AHM residues Glu262-Ser280. Towards the N-terminus of Mint1 acidic Glu267, Glu268, Asp269 and Glu276 each form complementary bonds with Munc18-1 residues, most notably with Arg388, Tyr411, and Lys415. These are supported by buried hydrophobic interactions of Mint1 Ile270 and Ile273. On the opposite side of the Mint1 α-helix C-terminus a network of bonds is formed between Mint1 Asp271 and Lys278, with Glu421, Lys425 and His429 of Munc18-1. To confirm the predicted binding site of Mint1 and Mint2 we mutated several residues in domain 3a of Munc18-1 including R388A, L395D, and H429A. In ITC experiments all three mutations showed a reduction in binding affinity and enthalpy, with L395D showing an almost complete loss of association (**Fig. 3E**). Altogether the Mint1 AHM is predicted to form an extensive complementary interface with Munc18-1, and we speculate that the relatively modest affinity between the two proteins may in part be due to the entropic cost of the induced α-helical folding of the AHM sequence.

As this work was being completed the Song and Feng labs published similar findings regarding the interaction of Munc18-1 with Mint proteins (Li *et al.*, 2023). The crystal structure of rat Mint1(227-303) bound to a complex of Munc18-1 and Sx1a was solved at 3.2 Å resolution, with electron density observed for Mint1 residues 266-283 associated with Munc18-1 domain 3b. This experimental structure correlates precisely with the region of human Mint1 we have mapped biochemically by truncations and mutagenesis and structurally with AlphaFold2. Based on their crystal structure, Li and colleagues termed the Munc18-1-binding Mint1 sequence the acidic α-helical motif (AHM) and we have also adopted this terminology. Overlay of the Munc18-1/Mint1 crystal structure with our top-ranked AlphaFold2 model shows an essentially identical binding mode

in all key details (**Fig. 4A**), and it is important to note the crystal structure was not included in the AlphaFold2 training set. One minor difference is that the AlphaFold2 predictions consistently model stable electrostatic contacts involving Mint1 Glu267 and Glu268. These are not seen in the crystal structure, and this is likely because these electrostatic contacts are relatively transient and thus not clearly observed in the modest resolution electron density maps. In addition to the crystal structure of Munc18-1/Sx1a bound to the Mint1 AHM, recently the structure of Munc18-1 in a ternary complex with Sx1a and the vesicular R-SNARE VAMP2 (also known as synaptobrevin) was also determined by cryoEM (Stepien et al., 2022). Similar to what was observed for yeast SM-family protein Vps33, this showed that Munc18-1 can provide a platform to template the assembly of the Qabc-SNARE/R-SNARE complex required for membrane fusion (Baker et al., 2015). Overlay of the complexes shows that the Mint1 and VAMP2 binding sites do not overlap and thus Mint1 could potentially associate simultaneously with both SNARE proteins (**Fig. 4B**). However, this does not preclude the possibility that protein dynamics or steric effects of the adjacent vesicle and plasma membranes could affect Mint1 interaction.

Mint1 binding to Munc18-1 allosterically modulates Sx1a interaction

To partly address the question of Munc18-1 dynamics in Mint1 association we examined the effects of domain3a deletions or the presence of Sx1a on their interaction. Previous studies have shown that the flexible hinge-loop region of Munc18-1 domain3a (residues 317-333) is required for efficient priming of secretory vesicles and controls the mobility of Sx1a and subsequent assembly of the SNARE complex (Han et al., 2013; Kasula et al., 2016; Martin et al., 2013). Structural studies of Munc18-1 show that this hinge-loop adopts a ‘closed’ or inhibitory conformation when Munc18-1 is bound to the Sx1a Habc and SNARE domains (Burkhardt et al., 2008; Burkhardt et al., 2011). Other structures of apo squid Munc18-1, rat Munc18-1 bound to a short Sx1a N-terminal peptide, and the recent cryoEM structure of Munc18-1 in ternary complex with Qa-SNARE Sx1a and R-SNARE VAMP2 show that domain3a can also adopt an ‘open’ conformation that is thought to be necessary for both releasing Sx1a inhibition and providing a platform for binding and assembly of other SNAREs (Bracher et al., 2000; Bracher and Weissenhorn, 2001; Hu et al., 2011; Stepien *et al.*, 2022). This is similar to what is seen when yeast SM protein Vps33 is bound to the Nyv1 SNARE (Baker *et al.*, 2015). Surprisingly, we find that deletion of the hinge-loop region in Munc18$^{\Delta 317\text{-}333}$, which has only a modest effect on Sx1a binding (Han *et al.*, 2013; Martin *et al.*, 2013), abolishes the binding of Mint1 both in GST pull-down and ITC experiments (**Fig. 5A, Fig. 5B**).

As Mint1 binds to Munc18-1 domain 3b, we hypothesized that the perturbed Mint1 interaction on deletion of the distal domain 3a hinge-loop might be due to altered structural dynamics in the combined domain3a/3b module. We therefore tested the binding of Sx1a to Munc18-1 in the absence and presence of the Mint1$^{261\text{-}282}$ peptide to determine if there were any changes in Sx1a affinity due to allosteric interactions. By GST pulldown of GST-Mint1 MID we did not observe a gross impact on the ability to bind Munc18-1 in the presence of the high affinity Sx1a ligand (**Fig. 5C**). This is in line

with the ability to co-crystallise the three proteins when excess Mint1 is present (Li *et al.*, 2023). However, when we quantified the binding affinity by ITC in the presence of Sx1a in complex with Munc18-1 we saw a small reduction in the affinity and enthalpy of binding of Mint1$^{261-282}$ peptide (**Fig. 5D; Table 2**). In reverse experiments, in the presence of a molar excess of Mint1$^{261-282}$ peptide we observe a reciprocal reduction in Sx1a binding affinity (K_d) from 7.9 nM to 269 nM (**Fig. 5E; Table 2**). This reduced affinity for Sx1a caused by Mint1 allostery is not seen when we use Munc18$^{\Delta 317-333}$ as expected (**Fig. 5F; Table 2**). Overall, the data indicates that Sx1a and Mint1 binding to Munc18-1 domains 3a and 3b respectively can allosterically regulate the interaction of the other protein. This could clearly have implications for a possible role of Mint proteins in Munc18-1 mediated SNARE assembly, which is a tightly regulated and highly dynamic process. Although we find that Mint1 affinity for Munc18-1 is reduced in the presence of Sx1a, this did not prevent the co-crystallisation of Mint1 bound to Munc18-1 by Li and colleagues in the presence of the Sx1a SNARE protein (Li *et al.*, 2023), although this is not inconsistent with the relatively modest reductions in affinity we observe.

Assessing the network of Mint interactions using AlphaFold2 based predictions

Following the successful modelling of the interaction with Munc18-1/2, we next explored the potential of AlphaFold2 to screen for, and map the binding sites of, other putative protein-protein interactors of the Mint1 and Mint2 neuronal proteins. Putative Mint1 and Mint2 interactors from the BioGRID repository (Oughtred et al., 2021), were screened for potential direct binding to Mint1 and Mint2 respectively using the ColabFold Batch implementation of AlphaFold2 (Mirdita *et al.*, 2022) (**Table S1; Table S2**). To assign a direct 'interactor' from these *in silico* analyses, we used an approach similar to recent work by Sifri and colleagues (Sifri et al., 2023). We initially assessed both the AlphaFold2-derived interfacial PTM (iPTM) score and the resultant PAE graphs which provide confidence metrics for the interactions between the proteins. For those with promising scores, we also examined the predicted structures in PyMOL to assess whether interacting regions involved the expected complementary hydrophobic, polar, and electrostatic contacts. To conserve GPU resource allocation, we initially generated only single predictions of each putative complex in AlphaFold2 in unsupervised batch mode. We found that a minimum iPTM score of ~0.3 combined with a strong signal in the PAE plot for inter-molecular structural correlation typically provided a useful indicator of a complex that was suitable for further assessment. In these cases, we subsequently ran at least three modelling experiments focusing on the specific domains of Mint1/Mint2 and the putative interactors that were predicted to interact with each other, to assess whether multiple predictions resulted in physically plausible structures that consistently aligned with each other in PyMOL (**Table S1; Table S2**).

As expected, these *in silico* interaction screens with AlphaFold2 correctly predicted several well characterised interactors, but also provided validation of a number of prospective binding partners so far only identified in high-throughput screens (**Figure S5; Figure S6; Table S1; Table S2**). Known interactors include the cytoplasmic NPxY motif of APP (Matos *et al.*, 2012; Xie *et al.*,

2013; Zhang *et al.*, 1997), and the CID sequence of CASK (Wu *et al.*, 2020; Zhang *et al.*, 2020) for which crystal structures have previously been determined. In addition, confident predictions were obtained for several other cytoplasmic sequences of transmembrane proteins previously identified to interact with Mint1 and/or Mint2 including lipoprotein receptors LRP1, LRP2 and LRP8 (Gotthardt *et al.*, 2000; He et al., 2007), calsyntenin-1 (CSTN1) (Araki et al., 2003) and KCNJ12 (Leonoudakis et al., 2004). These all utilize variations of the NPxY motif found in APP to associate with the Mint PTB domains (**Fig. 6A**). While LRP1, LRP2 and LRP8 each possess canonical NPxY sequences, CSTN1 and KCNJ12 are predicted to bind the same site of the PTB domain through divergent NPME and NELA sequences respectively. Several other proteins identified in BioGRID were predicted with reasonable confidence to associate directly with Mint1. A putative complex between the homeobox domain of HOXC9 and the PTB domain of Mint1 was modelled by AlphaFold2, via a surface distinct from the NPxY-binding groove. Putative novel interactions between the tandem PDZ domains of Mint1 were also predicted with the USP domain of USP22 (ubiquitin specific peptidase 22) and a C-terminal zinc-finger domain from the large protein WIZ (widely interspaced zinc finger-containing protein).

We chose four predicted interactions to describe in more detail; (i) the association of the Mint1 and Mint2 PTB domains with a peptide sequence from the coiled-coil protein Tight Junction Associated Protein 1 (TJAP1) also called Protein incorporated later into tight junctions (PILT) or tight junction protein 4 (TJP4)) (**Fig 6B, C**), (ii) the association of the Mint1 and Mint2 tandem PDZ domains with ADP-ribosylation factor (ARF) GTPases ARF3 and ARF4 (**Fig. 7A**), (iii) the interactions of the C-terminal sequence of the neurexin-1 (NRX1) receptor with the PDZ2 domain of Mint1/Mint2 (**Fig. 7B**), and (iv) lastly the interaction of an N-terminal YxxΦ motif in Mint1 with the μ3 subunit of the AP3 clathrin adaptor complex (**Fig. 7C**).

Outside of the canonical interactions of NPxY-related motifs with the Mint1 and Mint2 PTB domains, we observed a high confidence complex prediction involving a short peptide sequence in TJAP1 (, an interaction only previously reported in high-throughput proteomic screens (Huttlin et al., 2021) (**Fig. S6; Table S2**). The TJAP1 binding site is distinct from the binding groove of NPxY motifs, and subsequent predictions of the Mint1 and Mint2 PTB domains in the presence of both the NPxY motif of APP, and the peptide sequence from TJAP1 show highly consistent dual peptide interactions on opposite faces of the PTB domain (**Fig. 6B, C**). Both the APP and TJAP1-binding surfaces of Mint1 and Mint2 are highly conserved (**Fig. 6C**). The binding sequence of TJAP1 encompasses N-terminal residues ^{9}KPYRKAPPEHRELR^{22}, with buried aliphatic sidechains, and complementary electrostatic and hydrogen-bond contacts as shown in **Fig. 6D**. The sequence ^{16}PEHR^{19} is predicted to form a β-turn structure where the Pro16 sidechain forms a stacking interaction with the Arg19 guanidino group. These results suggest the Mint PTB domains are capable of recruiting proteins via two distinct peptide-motifs.

Mint2 was previously identified in a yeast two-hybrid screen for interactors of ARF3 (Hill et al., 2003). These screens identified fragments of Mint2 containing the tandem C-terminal PDZ

domains, and subsequent experiments showed that Mint1, Mint2 and Mint3 could all interact with both ARF3 and ARF4. AlphaFold2 predictions of full-length Mint2 complexed with ARF3 and ARF4 revealed a very high confidence interaction of the GTPases with the tandem PDZ domains, correlating precisely with the yeast two-hybrid studies (Hill *et al.*, 2003) (**Fig. S6; Table S2**). Predictions using the Mint1 and Mint2 PDZ domain sequences subsequently produced highly consistent complex structures with the two GTPases (**Fig. 7A**). The structure of activated ARF3-GTP bound to a bacterial toxin called MARTX was previously solved by X-ray crystallography (Lee et al., 2019). AlphaFold2 predicts ARF3 and ARF4 to be in the active GTP-Mg^{2+}-loaded conformation when bound to Mint1, and like the bacterial effector Mint1 and Mint2 primarily engage the switch 2 and interswitch regions of the GTPases, making little contact with the switch 1 region. The ARF GTPases bind an extensive and conserved surface with the interface composed of regions from both PDZ1 and PDZ2 domains in the tandem PDZ structure.

Although not listed in the BioGRID entries for Mint1 or Mint2, previous studies proposed that their PDZ domains interact with C-terminal sequences of NMDA receptors, kalirin-7, Neurexin-1 (NRX1), ApoER2/LRP8 and LDLR (Biederer and Sudhof, 2000; Gotthardt *et al.*, 2000; Jones *et al.*, 2014; Minami *et al.*, 2010; Motodate *et al.*, 2019). PDZ domains are small scaffolds that bind to PDZ binding motifs (PDZbms) found at the C-terminus of their interacting proteins. They typically fall in three classes; Type 1 with consensus [S/T]xΦ (x = any amino acid; Φ = hydrophobic amino acid), Type 2 with consensus ΦxΦ, and Type 3 with consensus [E/D]xΦ .(Hung and Sheng, 2002; Nourry et al., 2003). We used AlphaFold2 to predict the interaction of the Mint1 and Mint2 PDZ domains with the C-terminal sequence of NRX1, which conforms to a Type 2 PDZbm. This confidently predicted an interaction between the C-terminal ^{1471}KDKEYYV^{1477} NRX1 sequence with the second PDZ2 domain of the PDZ1-PDZ2 tandem structure (**Fig. 7B**). The C-terminal Val1477 side chain (position '0' in standard PDZbm nomenclature) docks in a complementary hydrophobic pocket with the terminal carboxyl group hydrogen bonding with the backbone amides of Mint1 Leu759 and Gly760. The NRX1 Tyr1475 and Tyr1476 side chains at positions -1 and -2 pack into complementary surface grooves, while both main-chain and side-hydrogen bonds upstream of the C-terminal interaction provide further specificity. This requires experimental validation, but combined with the fact that the C-terminal Mint1 sequence PVYI (PLIY in Mint2) can form an intramolecular interaction with its own PDZ1 domain (Long et al., 2005) it suggests that the PDZ2 domain of the Mint proteins provides the major platform for recruiting PDZbm-containing ligands.

The last predicted interaction we examined in detail was that of Mint1 with the μ3 subunit of the tetrameric AP3 clathrin adaptor complex (**Fig. 7C**), another unexpected association reported in the same high-throughput screens as TJAP1 (Huttlin *et al.*, 2021). The μ3 subunit has an N-terminal longin domain that embeds it within the AP3 tetramer, and a C-terminal μ-homology domain (MHD) that associates with YxxΦ tyrosine-based motifs (where Φ is a bulky hydrophobic residue), typically in transmembrane cargos for sorting from endosomes to lysosomal compartments (Mardones et al., 2013; Sanger et al., 2019). The predicted structure of the Mint1 ^{298}YEEI^{301} sequence closely

370 resembles the crystal structure of the TGN38 motif YQRL bound to the rat μ3 MHD, with both Tyr298
371 and Ile301 inserting into complementary surface pockets as typically seen for YxxΦ motifs. We also
372 tested AlphaFold2 predictions of the Mint1 sequence with other μ-subunits from AP1, AP2, AP4 and
373 AP5. While μ1, μ2 and μ4 proteins were each predicted to interact, the iPTM confidence scores were
374 much lower, and AP5 was not predicted to bind at all.

375 While we have focused on proteins that *are* predicted to bind to Mint1/Mint2, it is notable that
376 from the list of putative BioGRID interactors the majority are *not* likely to associate directly with the
377 Mint adaptors, including many that have previously been identified using methods such as co-
378 immunoprecipitations (**Table S1; Table S2**). In some case this could be due to limitations with the
379 predictive ability of AlphaFold2; However it also likely indicates that many of the proteins reported in
380 BioGRID either bind indirectly (via other proteins not included in our binary predictions) or are non-
381 specific interactions detected by the proteomics methods.

382 **DISCUSSION**

383 The interaction of Munc18-1 with Mint proteins has long been known to be important for synaptic
384 neurotransmitter and hormonal release through the regulation of SNARE-mediated vesicle fusion.
385 While the molecular basis for the scaffolding and trafficking of the APP transmembrane protein and
386 CASK kinase have been well characterised (Matos *et al.*, 2012; Wu *et al.*, 2020; Xie *et al.*, 2013;
387 Zhang *et al.*, 1997; Zhang *et al.*, 2020), the mechanism by which Mint bind to Munc18-1 was
388 unknown. In this work, and in a related study by Li and colleagues (Li *et al.*, 2023), the interaction is
389 revealed to be via the binding of Munc18-1 domain3b via a conserved α-helical motif (AHM) in the
390 N-terminal unstructured domains of the Mint1 and Mint2 neuronal homologues. The binding surface
391 on Munc18-1 is distinct from its known binding sites for the Sx1a and VAMP2 SNARE proteins,
392 although we find there is a small but significant reduction in the binding affinity of Sx1a in the
393 presence of the Mint1 AHM. We speculate this could point to a role of Mint proteins in regulating the
394 SNARE complex dynamic templating activity of Munc18-1 which will be worth future investigation.

395 The AHM sequence found in Mint1 and Mint2 is well conserved across many species,
396 although it appears not to be present in some organisms such as nematodes and flies. Further, it
397 may be relatively specific to the Mint proteins, with few if any other proteins possessing similar motifs.
398 We scanned the human genome using ScanProsite and did not find any other proteins with highly
399 similar sequences. Li and colleagues reported potential AHMs in Munc13-1, Bassoon, and Atg16L,
400 although no binding was detected using the putative motif from Munc13-1 by ITC (Li *et al.*, 2023).
401 Future proteomic studies of Munc18-1 using specific domain3b mutations may reveal the existence
402 of other proteins able to bind this site, but there are unlikely to be a large number. Like the CASK-
403 binding CID sequence in Mint1, the Mint1 and Mint2 AHM sequences lie within their extended and
404 intrinsically unstructured N-terminal domain, likely adopting their α-helical structures via induced
405 folding upon Munc18-1 interaction. This may explain the relatively modest binding affinity for
406 Munc18-1 despite the reasonably large binding surface. The interaction between these proteins is
407 thus likely highly context dependent, relying on both their specific coupling as well as their
408 colocalization at the membrane surface and likely clustering with other proteins such as the SNAREs,
409 APP, neurexins, and potentially small GTPases like ARF3.

410 In addition to dissecting the mechanism of Mint1 and Mint2 interaction with Munc18-1, we
411 have used machine-learning based structure prediction with AlphaFold2 to assess the broader
412 interactome of the Mint proteins. These predictions provide useful insights into those interactions
413 that are likely to be directly mediated by the Mint proteins. Our results provide an example of how
414 AlphaFold2 (and similar algorithms) can be used to provide confidence in the plausibility of
415 complexes identified in larger proteomic datasets (Burke et al., 2023; Gao et al., 2022a; Gao et al.,
416 2022b; Humphreys et al., 2021; Sifri *et al.*, 2023; Yu et al., 2023). Such an approach has the potential
417 to inform and accelerate subsequent experimental validation of molecular complexes detected in
418 high-throughput screens, by providing much greater confidence as to which hits represent specific
419 interactions.

Apart from the expected predictions of CASK and APP, for which previous crystal structures are available, there were several other notable complexes that were confidently modelled by AlphaFold2 in this study. A number of proteins have been reported to interact with the PDZ domains of Mint1 and Mint2 via C-terminal PDZbms, including calcium channels (Maximov et al., 1999), kalirin-7 (Jones *et al.*, 2014; Penzes, 2001), NMDA receptors (Motodate *et al.*, 2019) and NRX1 (Biederer and Sudhof, 2000; Dean and Dresbach, 2006). Furthermore, the C-terminus of Mint proteins can form an intramolecular interaction with the PDZ1 domain, effectively acting as an autoinhibitory sequence of PDZ1 (Long *et al.*, 2005). Taking NRX1 as an example, we found that its Type II PDZbm was predicted to interact with the PDZ2 domain, in the canonical β-strand orientation. Since other neurexin homologues share the same C-terminal sequence, this suggests they may use the same binding mechanism. This hypothesis, as well as whether the second PDZ2 domain is bound by other PDZbms warrants further investigation.

One novel Mint interactor predicted by AlphaFold2 was TJAP1, which was identified in high-throughput proteomic screens with all three Mint homologues (Huttlin *et al.*, 2021). TJAP1 has an N-terminal unstructured region, which is predicted here to interact with Mint PTB domains, a central-coil region predicted by AlphaFold2 to form a homodimer (not shown), and an extended C-terminal unstructured and Proline-rich domain. The precise function of TJAP1 is essentially unknown, although it was identified in yeast two-hybrid assays to bind the GTPase ARF6 (Tamaki et al., 2012) and discs large-2 (Dlg-2/PSD93) (Kawabe et al., 2001), a member of the membrane-associated guanylate kinase (MAGUK) protein family that includes CASK (Ye et al., 2018). TJAP1 is localised to both the Golgi and tight junctions (Kawabe *et al.*, 2001; Tamaki *et al.*, 2012), and the putative interaction with the TJAP1 N-terminal peptide sequence is confidently predicted with not only the neuronal Mint1 and Mint2 proteins but also the ubiquitous Mint3 protein (not shown) so it is possible that the association is important in cell types other than neurons.

Similar to TJAP1, the ARF3 and ARF4 small GTPases were originally identified to bind Mint proteins in yeast two-hybrid screens (Hill *et al.*, 2003), however no subsequent studies have examined the mechanism or functional role of these interactions. Our modelling indicates a conserved binding site involving the PDZ1 and PDZ2 tandem domains of the Mint proteins, which support the original yeast two-hybrid mapping experiments. ARF3 is highly enriched in the brain, and both proteins play a role in maintaining recycling endosome morphology and integrity (Kondo et al., 2012; Nakai et al., 2013). Interestingly ARF3 mutations have recently been found in patients with neurodevelopmental disorders characterised by brain abnormalities, microcephaly and seizures (Fasano et al., 2022; Sakamoto et al., 2021). It is tempting to speculate these disorders overlap with synaptopathies caused by mutations in Munc18-1, CASK and other synaptic proteins, therefore suggesting a role in the synaptic vesicle trafficking pathways that could in part be mediated through the Mint proteins.

The last predicted interaction we examined was that of Mint1 with the AP3 clathrin adaptor complex. This involves binding of the AP3 μ3A domain with a canonical YxxΦ sequence in the Mint1

N-terminal region (not present in Mint2 or Mint3). It would indicate that the Mint1 N-terminus has at least two functions distinct from the other Mint isoforms; the ability to bind CASK, and the potential to couple Mint1 and bound proteins (such as APP or neurexins for example) into AP3 mediated transport structures. AP3 is primarily found on endosomes where it mediates trafficking to lysosomes and lysosome-related organelles (Sanger *et al.*, 2019), and depending on specific subunit isoforms has important roles in axonal transport and synaptic function by regulating the reformation of synaptic vesicles from endosomes derived from bulk synaptic endocytosis (Blumstein et al., 2001; Evstratova et al., 2014; Li et al., 2016; Newell-Litwa et al., 2010; Seong et al., 2005; Shetty et al., 2013; Voglmaier et al., 2006). Similar to ARF3, mutations in neuronal AP3 isoforms can lead to neurodevelopmental disorders with some similar features to Synaptopathies, suggesting a potential functional overlap of Mint1 and AP3 in synaptic integrity (Ammann et al., 2016; Assoum et al., 2016).

A model for Mint1 is shown in **Fig. 8** summarising the known and predicted interactions mediated by this scaffold protein. **Fig. 8A** shows an AlphaFold2 prediction of the full-length protein highlighting binding sequences and domains of the protein and underlines the highly extended nature of the N-terminal intrinsically disordered domain containing the Munc18-1 binding AHM as well as binding motifs for the AP3 adaptor and CASK. **Fig. 8B** is a cartoon summary of the interactions described above and highlights the overall scaffolding function of this protein. From our biophysical and biochemical studies, we speculate that the reduced affinity of Sx1a for Munc18-1 in the presence of the Mint AHM sequence could lead to an enhancement of SNARE assembly mediated by Munc18-1 templating, although this will require significant further validation. A final caveat to this model is that it does not account for temporal regulation of the various interactions, the impact of posttranslational modifications or the cellular context where each interaction is likely to occur including the plasma membrane and other organelles such as endosomes and the Golgi.

In summary, we have mapped and characterised the specific association of the neuronal Mint1 and Mint2 proteins with the SNARE regulatory protein Munc18-1 providing a high-resolution snapshot for how these key synaptic proteins interact with other, confirming and extending recent related work (Li *et al.*, 2023). This study further emphasises the ability of AlphaFold2, at least in many instances, to predict protein-peptide interactions with a high degree of accuracy. By applying a wider set of systematic analyses, our work has revealed likely modes of interaction between the Mint proteins and a variety of known and novel effectors, which provides a foundation for future mechanistic studies of their important role in synaptic activity.

490 **METHODS**

491 ***Antibodies, plasmids and peptides***

492 Human Mint1 sequences for bacterial expression were codon optimised and sub-cloned into the
493 pGEX4T-2 plasmid by Genscript (USA). The constructs generated were GST-tagged Mint1(226-
494 314)(MID), Mint1(261-272), Mint1(261-282), Mint1(226-289), Mint1(222-314), Mint1(237-289).
495 Human Mint1 open reading frame and mutant Mint1(D269A/I270A) were obtained from Genscript
496 and cloned into the pcDNA3.1-N-eGFP. All synthetic peptides were purchased from Genscript (USA).
497 GFP polyclonal antibody and Goat anti-mouse secondary antibody were purchased from Thermo
498 Fisher and Mouse monoclonal anti-munc18-1 was purchased from BD biosciences.

499

500 ***Recombinant protein expression and purification***

501 All proteins were expressed in *Escherichia coli* Rosetta™(DE3) cells. GST-Mint1 (226-314, the
502 Munc18-1 interacting domain (MID)), containing pGEX4T-2 vector was transformed into Rosetta
503 cells and plated on a LB/Agar plate supplemented with Ampicillin (0.1mg/mL). Single colony was
504 then used to inoculate 50 mL of LB medium containing Ampicillin (0.1 mg/mL). and the culture was
505 grown overnight at 37 ^{o}C with shaking at 180 rpm. The following day, 1L of LB medium containing
506 antibiotics Ampicillin (0.1 mg/mL) and Chloramphenicol (0.034 mg/mL) was inoculated using 10 mL
507 of the overnight culture. Cells were then grown at 37 ^{o}C with shaking at 180 rpm to an optical density
508 of 0.7-0.8 at 600 nm and the protein expression was induced by adding 0.5 mM IPTG (isopropyl-β-
509 D-thiogalactopyranoside). Expression cultures were incubated at 20 ^{o}C overnight. And the cells were
510 harvested next day by centrifugation at 4000 rpm for 15 min using Beckman rotor JLA 8.100. Cell
511 pellets were resuspended in 20 mL (for cell pellet from 1L) of lysis buffer (50 mM Tris, pH 8.0, 500
512 mM NaCl, 10% glycerol, 1 mM DTT, Benzamidine (0.1mg/mL), and Dnase (0.1 mg/mL)).
513 Resuspended cells were further lysed by using the cell disrupter (Constant systems, LTD, UK , TS-
514 Series) and the soluble fraction containing GST-Mint1 was separated from cell debris by
515 centrifugation at 18,000 rpm for 30 min at 4 ^{o}C. The soluble fraction was first purified by affinity
516 chromatography using glutathione-Sepharose resin and the GST-Mint1 was eluted using 50 mM Tris,
517 pH 8.0, 500 mM NaCl, 10% glycerol, 1 mM DTT buffer and the protein containing fractions were
518 concentrated and further purified by gel filtration chromatography (Superdex 75 (16/600), GE
519 Healthcare). GST-Mint1 containing fractions were analysed by SDS PAGE. All the other GST-Mint1
520 constructs (GST Mint1 261-272, 261-282, 226-289, 222-314, 237-289) were also expressed and
521 purified as described above.

522 For GFP-nanotrap preparation, the plasmid pOPINE harbouring His-SUMO-GFP-nanotrap
523 was transformed into *Escherichia coli* Bl21 (DE3) cells and plated on a LB/Agar plate supplemented
524 with Ampicillin. GFP-nanotrap refers to the camelid-derived nanobody specific for GFP (Kubala et
525 al., 2010). The expression and lysis of cells were carried out as described above. The supernatant
526 containing GFP nano trap was first purified by affinity chromatography using Talon resin equilibrated
527 with 50 mM Tris (pH 8.0), 500 mM NaCl, 10 % Glycerol and protein bound to the column was eluted

528 using elution buffer containing 50 mM Tris (pH 8.0), 500 mM NaCl, 10 % Glycerol, 300 mM Imidazole.
529 The fractions containing GFP-nanotrap was combined, concentrated and loaded on to a Superdex
530 75 (16/60) column equilibrated with 50 mM Hepes (pH 7.5), 200 mM NaCl, 0.5 mM TCEP (tris(2-
531 carboxyethyl)phosphine). The fractions containing the protein were analysed by SDS PAGE,
532 combined, and concentrated to the desired concentration. Rat Sx1a ($Sx1_{1-261}$-His), Munc18-1-His
533 and Munc18-$1^{\Delta 317-333}$ were also expressed and purified to homogeneity as described Hu et al (Hu *et*
534 *al.*, 2011).
535
536 ***PC12 Cell culture and Transfection:***
537 Neurosecretory cell line, Pheochromocytoma cells (PC12), were cultured at 37 °C/5% CO_2 in normal
538 culture media (Dulbecco's modified Eagle's medium (High glucose, pyruvate, Gibco, Cat#11995),
539 7.2% Heat-inactivated Foetal Bovine Serum (Gibco), 7.2% Heat-inactivated Horse Serum (Gibco),
540 1x GlutaMAX™ supplement (Gibco, Cat# 35050061)). Cells were transfected using Lipofectamine™
541 LTX (Invitrogen, Cat#15338100) as per manufacturer's instructions. For co-IP experiments PC12
542 cells 4 x 10^6 cells were cultured in 10 cm culture dishes (TPP Techno Plastic Products AG) coated
543 with 0.1 mg/mL Poly-D-Lysine (Sigma, P2636). For each condition 15.3 μg plasmid DNA was used
544 per 10 cm dish and 2x 10 cm dishes were pooled for experiments. PC12 cells were transfected with
545 either pEGFP-N1 (GFP Control), pcDNA3.1-N-eGFP hMint1 WT or pcDNA3.1-N-eGFP hMint1
546 DI/AA mutant, and 48hr post transfected cell pellets were collected for subsequent co-IP/GFP Trap.
547
548 ***Co-immunoprecipitation (Co-IP)***
549 PC12 cells containing EGFP, GFP- hMint1 (WT), GFP hMint1 DI/AA were lysed on ice using buffer
550 composed of 20 mM Hepes, 50 mM NaCl, 1% Triton, 1 mM DTT, DNAse and a tablet of protease
551 inhibitor cocktail. To further enhance the Lysis, the lysate was aspirated through a small needle
552 approximately 10 times. The lysate was then centrifuged at 17,000 *g* for 15 minutes to separate the
553 cellular debris from the supernatant containing the soluble proteins. 50 μl of GFP nano trap coupled
554 to NHS activated Sepharose 4 beads were added to each of the three supernatants containing GFP,
555 GFP-hMint1 WT and GFP-hMint1 DI/AA. The supernatant-bead mixtures were incubated for 2 hours
556 at 4 °C while shaking, and then the beads were spun down by at 5000 *g* for 2 minutes to remove the
557 unbound proteins. The bead samples were washed three times using the lysis buffer, and 50 μl of
558 SDS sample buffer was added to each sample. The beads, containing the immunoprecipitated
559 proteins were boiled at 95 °C for 5 minutes to elute the bound proteins and resolved using Western
560 immunoblotting. GFP and Munc18a proteins were detected using anti-GFP mouse and anti-
561 Munc18a mouse as primary antibodies respectively and Goat anti-mouse antibody as the secondary
562 antibody. The final imaging was performed using ECL and Odyssey infrared imaging system (LI-
563 COR).
564
565

566 ***Isothermal titration calorimetry (ITC)***

567 For ITC, the peptides were weighed and initially dissolved in the working buffer to make a stock
568 concentration of 2 mM. ITC experiments were carried out on Microcal iTC200 at 25 ^{o}C. GST-Mint1
569 and all the other proteins used in the experiments were buffer exchanged into 50 mM Tris, (pH 8.0),
570 200 mM NaCl by gel filtration prior to ITC. GST-Mint1 (1 mM) or Mint1 synthetic peptide (0.7 mM)
571 were titrated into Munc18-1-His (50 μM). The binding parameters, equilibrium constant K_a ($1/K_d$),
572 stoichiometry (n) and the enthalpy (ΔH) were determined by processing the ITC data using ORIGIN
573 7.0 software. The equation, $\Delta G = \Delta H - T\Delta S$ was used to calculate the Gibbs free energy (ΔG) and
574 all the experiments were performed in triplicate to calculate the standard error of the mean (SEM)
575 for thermodynamic parameters.

576

577 ***Pull down assays***

578 Pull down assays were carried out using GST-Mint1 and Munc18-1-His. 0.5 nmol of GST-Mint1 was
579 mixed with 1 nmol of Munc18-1-His in 500 μL of pull down buffer (50 mM Tris pH 8.0, 200 mM NaCl,
580 1mM DTT, 0.1% IGEPAL) and incubated for 30 min on a rotating holder at 4 ^{o}C. The protein mixture
581 was then centrifuged at full speed for 5 min and 50 μL of glutathione Sepharose resin pre-equilibrated
582 in pull down buffer was added. The protein mix with the resin was incubated further 30 min at 4 ^{o}C
583 on a rotating holder and at the end of the incubation, the beads were spun down at 5000 rpm for 30
584 sec. The supernatant containing the unbound protein is pipetted off and the beads with the bound
585 protein was washed 4 times with 1 mL of pull down buffer. 50 μL of SDS sample buffer was added
586 to the beads and analysed by SDS-PAGE for bound proteins.

587

588 ***Protein structural prediction, modelling and visualisation***

589 All protein models were generated using AlphaFold2 Multimer (Evans *et al.*, 2022; Jumper *et al.*,
590 2021) implemented in the Colabfold interface available on the Google Colab platform (Mirdita *et al.*,
591 2022). For each modelling experiment ColabFold was executed using default settings where multiple
592 sequence alignments were generated with MMseqs2 (Mirdita et al., 2019). For all final models
593 displayed in this manuscript, structural relaxation of peptide geometry was performed with AMBER
594 (Hornak et al., 2006). For all modelling experiments, we assessed (i) the prediction confidence
595 measures (pLDDT and interfacial iPTM scores), (ii) the plots of the predicted alignment errors (PAE)
596 and (iii) backbone alignments of the final structures. For modelling of the complex between Munc18-
597 1 and Mint1 we initially predicted the complex between full-length proteins and identified a high-
598 confidence binding sequence in the N-terminal region of Mint1 that correlated precisely with the
599 binding motif identified in our biochemical experiments. Based on this initial model and our
600 biochemical mapping of the minimal Mint1 sequence for Munc18-1 binding we performed multiple
601 independent predictions using a shorter peptide region, combined with AMBER energy minimization
602 to optimize amino acid stereochemistry.

603 For interactome-wide analysis of other protein-protein interactors of Mint1 and Mint2 we
604 obtained a list of putative interactors from the BioGRID repository (Oughtred *et al.*, 2021), and
605 predicted whether they formed direct complexes using the ColabFold Batch implementation of
606 AlphaFold2 (Mirdita *et al.*, 2022) (**Table S1; Table S2**). To assign a direct 'interactor' from these *in*
607 *silico* analyses we used an approach similar to recent work by Sifri and colleagues (Sifri *et al.*, 2023).
608 We initially assessed both the AlphaFold2-derived interfacial PTM (iPTM) score and the resultant
609 PAE graphs which provide confidence metrics for the interactions between the proteins. For those
610 with promising scores we also examined the predicted structures in PyMOL to assess whether
611 interacting regions involved the expected complementary hydrophobic, polar, and electrostatic
612 contacts. To conserve GPU resource allocation, we initially generated only single predictions of each
613 putative complex in AlphaFold2 in unsupervised batch mode. We found that a minimum iPTM score
614 of ~0.3 combined with a strong signal in the PAE plot for inter-molecular structural correlation
615 typically provided a useful indicator of a complex that was suitable for further assessment. In these
616 cases, we subsequently ran at least three modelling experiments focusing on the specific domains
617 of Mint1/Mint2 and the putative interactors that were predicted to interact with each other, to assess
618 whether multiple predictions resulted in physically plausible structures that consistently aligned with
619 each other in PyMOL (**Table S1; Table S2**). Sequence conservation across PDB models was
620 mapped with Consurf (Ashkenazy et al., 2016). All structural images were made with Pymol
621 (Schrodinger, USA; https://pymol.org/2/).
622

Acknowledgements

This work was supported by grants from the National Health and Medical Research Council of Australia (NHMRC) (APP1138083 and APP1139316) to B.M.C and FAM. B.M.C is supported by an NHMRC Investigator Grant and previous Senior Research Fellowship (APP2016410 and APP1136021). F.A.M is supported by an NHMRC Senior Research Fellowship (GNT1155794). We would like to thank Lionel Louiset, Ailisa Blum, Pranesh Padmanabahn and Jenny Martin for their assistance with this work, including initial mammalian construct testing, funding contributions and supervision of students.

Author contributions

B.M.C. designed research with some input of F.A.M; S.W. and E.L. performed ITC analysis, pulldown assays and S.W. and B.M.C. performed AlphaFold2 modelling; S.W. and R.S.G performed coimmunoprecipitation assays; F.A.M. and B.M.C acquired funding and provided student supervision; and S.W., R.S.G., F.A.M. and B.M.C wrote the paper with input by all authors.

Conflict of interest

Authors declare that they have no conflict of interest.

643 **References**

644

645 Ammann, S., Schulz, A., Krageloh-Mann, I., Dieckmann, N.M., Niethammer, K., Fuchs, S., Eckl,
646 K.M., Plank, R., Werner, R., Altmuller, J., et al. (2016). Mutations in AP3D1 associated with
647 immunodeficiency and seizures define a new type of Hermansky-Pudlak syndrome. Blood *127*, 997-
648 1006. 10.1182/blood-2015-09-671636.

649 Araki, Y., Tomita, S., Yamaguchi, H., Miyagi, N., Sumioka, A., Kirino, Y., and Suzuki, T. (2003).
650 Novel cadherin-related membrane proteins, Alcadeins, enhance the X11-like protein-mediated
651 stabilization of amyloid beta-protein precursor metabolism. J Biol Chem *278*, 49448-49458.
652 10.1074/jbc.M306024200.

653 Ashkenazy, H., Abadi, S., Martz, E., Chay, O., Mayrose, I., Pupko, T., and Ben-Tal, N. (2016).
654 ConSurf 2016: an improved methodology to estimate and visualize evolutionary conservation in
655 macromolecules. Nucleic Acids Res *44*, W344-350. 10.1093/nar/gkw408.

656 Assoum, M., Philippe, C., Isidor, B., Perrin, L., Makrythanasis, P., Sondheimer, N., Paris, C., Douglas,
657 J., Lesca, G., Antonarakis, S., et al. (2016). Autosomal-Recessive Mutations in AP3B2, Adaptor-
658 Related Protein Complex 3 Beta 2 Subunit, Cause an Early-Onset Epileptic Encephalopathy with
659 Optic Atrophy. Am J Hum Genet *99*, 1368-1376. 10.1016/j.ajhg.2016.10.009.

660 Babatz, T.D., Kumar, R.A., Sudi, J., Dobyns, W.B., and Christian, S.L. (2009). Copy number and
661 sequence variants implicate APBA2 as an autism candidate gene. Autism Res *2*, 359-364.
662 10.1002/aur.107.

663 Baker, R.W., Jeffrey, P.D., Zick, M., Phillips, B.P., Wickner, W.T., and Hughson, F.M. (2015). A direct
664 role for the Sec1/Munc18-family protein Vps33 as a template for SNARE assembly. Science *349*,
665 1111-1114. 10.1126/science.aac7906.

666 Becamel, C., Alonso, G., Galeotti, N., Demey, E., Jouin, P., Ullmer, C., Dumuis, A., Bockaert, J., and
667 Marin, P. (2002). Synaptic multiprotein complexes associated with 5-HT(2C) receptors: a proteomic
668 approach. EMBO J *21*, 2332-2342. 10.1093/emboj/21.10.2332.

669 Biederer, T., Cao, X., Sudhof, T.C., and Liu, X. (2002). Regulation of APP-dependent transcription
670 complexes by Mint/X11s: differential functions of Mint isoforms. J Neurosci *22*, 7340-7351.

671 Biederer, T., and Sudhof, T.C. (2000). Mints as adaptors. Direct binding to neurexins and recruitment
672 of munc18. J Biol Chem *275*, 39803-39806. 10.1074/jbc.C000656200.

673 Blumstein, J., Faundez, V., Nakatsu, F., Saito, T., Ohno, H., and Kelly, R.B. (2001). The neuronal
674 form of adaptor protein-3 is required for synaptic vesicle formation from endosomes. J Neurosci *21*,
675 8034-8042. 10.1523/JNEUROSCI.21-20-08034.2001.

676 Borg, J.P., Ooi, J., Levy, E., and Margolis, B. (1996). The phosphotyrosine interaction domains of
677 X11 and FE65 bind to distinct sites on the YENPTY motif of amyloid precursor protein. Mol Cell Biol
678 *16*, 6229-6241. 10.1128/mcb.16.11.6229.

679 Borg, J.P., Straight, S.W., Kaech, S.M., de Taddeo-Borg, M., Kroon, D.E., Karnak, D., Turner, R.S.,
680 Kim, S.K., and Margolis, B. (1998). Identification of an evolutionarily conserved heterotrimeric protein
681 complex involved in protein targeting. J Biol Chem *273*, 31633-31636. 10.1074/jbc.273.48.31633.

682 Bracher, A., Perrakis, A., Dresbach, T., Betz, H., and Weissenhorn, W. (2000). The X-ray crystal
683 structure of neuronal Sec1 from squid sheds new light on the role of this protein in exocytosis. Struct
684 Fold Des *8*, 685-694. Doi 10.1016/S0969-2126(00)00156-8.

685 Bracher, A., and Weissenhorn, W. (2001). Crystal structures of neuronal squid Sec1 implicate inter-
686 domain hinge movement in the release of t-SNAREs. J Mol Biol *306*, 7-13. 10.1006/jmbi.2000.4347.

Burke, D.F., Bryant, P., Barrio-Hernandez, I., Memon, D., Pozzati, G., Shenoy, A., Zhu, W., Dunham, A.S., Albanese, P., Keller, A., et al. (2023). Towards a structurally resolved human protein interaction network. Nat Struct Mol Biol. 10.1038/s41594-022-00910-8.

Burkhardt, P., Hattendorf, D.A., Weis, W.I., and Fasshauer, D. (2008). Munc18a controls SNARE assembly through its interaction with the syntaxin N-peptide. EMBO J *27*, 923-933. 10.1038/emboj.2008.37.

Burkhardt, P., Stegmann, C.M., Cooper, B., Kloepper, T.H., Imig, C., Varoqueaux, F., Wahl, M.C., and Fasshauer, D. (2011). Primordial neurosecretory apparatus identified in the choanoflagellate Monosiga brevicollis. Proc Natl Acad Sci U S A *108*, 15264-15269. 10.1073/pnas.1106189108.

Caster, A.H., and Kahn, R.A. (2013). Recruitment of the Mint3 adaptor is necessary for export of the amyloid precursor protein (APP) from the Golgi complex. J Biol Chem *288*, 28567-28580. 10.1074/jbc.M113.481101.

Chaufty, J., Sullivan, S.E., and Ho, A. (2012). Intracellular amyloid precursor protein sorting and amyloid-beta secretion are regulated by Src-mediated phosphorylation of Mint2. J Neurosci *32*, 9613-9625. 10.1523/JNEUROSCI.0602-12.2012.

Christie, M.P., Whitten, A.E., King, G.J., Hu, S.H., Jarrott, R.J., Chen, K.E., Duff, A.P., Callow, P., Collins, B.M., James, D.E., and Martin, J.L. (2012). Low-resolution solution structures of Munc18:Syntaxin protein complexes indicate an open binding mode driven by the Syntaxin N-peptide. Proc Natl Acad Sci U S A *109*, 9816-9821. 10.1073/pnas.1116975109.

Corpet, F., Gouzy, J., and Kahn, D. (1999). Browsing protein families via the 'Rich Family Description' format. Bioinformatics *15*, 1020-1027. 10.1093/bioinformatics/15.12.1020.

Dean, C., and Dresbach, T. (2006). Neuroligins and neurexins: linking cell adhesion, synapse formation and cognitive function. Trends Neurosci *29*, 21-29. 10.1016/j.tins.2005.11.003.

Diella, F., Haslam, N., Chica, C., Budd, A., Michael, S., Brown, N.P., Trave, G., and Gibson, T.J. (2008). Understanding eukaryotic linear motifs and their role in cell signaling and regulation. Front Biosci *13*, 6580-6603.

Dunning, C.J., Black, H.L., Andrews, K.L., Davenport, E.C., Conboy, M., Chawla, S., Dowle, A.A., Ashford, D., Thomas, J.R., and Evans, G.J. (2016). Multisite tyrosine phosphorylation of the N-terminus of Mint1/X11alpha by Src kinase regulates the trafficking of amyloid precursor protein. J Neurochem *137*, 518-527. 10.1111/jnc.13571.

Evans, R., O'Neill, M., Pritzel, A., Antropova, N., Senior, A., Green, T., Žídek, A., Bates, R., Blackwell, S., Yim, J., et al. (2022). Protein complex prediction with AlphaFold-Multimer. bioRxiv, 2021.2010.2004.463034. 10.1101/2021.10.04.463034.

Evstratova, A., Chamberland, S., Faundez, V., and Toth, K. (2014). Vesicles derived via AP-3-dependent recycling contribute to asynchronous release and influence information transfer. Nat Commun *5*, 5530. 10.1038/ncomms6530.

Fasano, G., Muto, V., Radio, F.C., Venditti, M., Mosaddeghzadeh, N., Coppola, S., Paradisi, G., Zara, E., Bazgir, F., Ziegler, A., et al. (2022). Dominant ARF3 variants disrupt Golgi integrity and cause a neurodevelopmental disorder recapitulated in zebrafish. Nat Commun *13*, 6841. 10.1038/s41467-022-34354-x.

Gao, M., Nakajima An, D., Parks, J.M., and Skolnick, J. (2022a). AF2Complex predicts direct physical interactions in multimeric proteins with deep learning. Nat Commun *13*, 1744. 10.1038/s41467-022-29394-2.

730 Gao, M., Nakajima An, D., and Skolnick, J. (2022b). Deep learning-driven insights into super protein
731 complexes for outer membrane protein biogenesis in bacteria. Elife *11*. 10.7554/eLife.82885.

732 Gotthardt, M., Trommsdorff, M., Nevitt, M.F., Shelton, J., Richardson, J.A., Stockinger, W., Nimpf,
733 J., and Herz, J. (2000). Interactions of the low density lipoprotein receptor gene family with cytosolic
734 adaptor and scaffold proteins suggest diverse biological functions in cellular communication and
735 signal transduction. J Biol Chem *275*, 25616-25624. 10.1074/jbc.M000955200.

736 Graham, M.E., Prescott, G.R., Johnson, J.R., Jones, M., Walmesley, A., Haynes, L.P., Morgan, A.,
737 Burgoyne, R.D., and Barclay, J.W. (2011). Structure-function study of mammalian Munc18-1 and C.
738 elegans UNC-18 implicates domain 3b in the regulation of exocytosis. PLoS One *6*, e17999.
739 10.1371/journal.pone.0017999.

740 Gross, G.G., Lone, G.M., Leung, L.K., Hartenstein, V., and Guo, M. (2013). X11/Mint genes control
741 polarized localization of axonal membrane proteins in vivo. J Neurosci *33*, 8575-8586.
742 10.1523/JNEUROSCI.5749-12.2013.

743 Han, G.A., Bin, N.R., Kang, S.Y., Han, L., and Sugita, S. (2013). Domain 3a of Munc18-1 plays a
744 crucial role at the priming stage of exocytosis. J Cell Sci *126*, 2361-2371. 10.1242/jcs.126862.

745 Han, G.A., Park, S., Bin, N.R., Jung, C.H., Kim, B., Chandrasegaram, P., Matsuda, M., Riadi, I., Han,
746 L., and Sugita, S. (2014). A pivotal role for pro-335 in balancing the dual functions of Munc18-1
747 domain-3a in regulated exocytosis. J Biol Chem *289*, 33617-33628. 10.1074/jbc.M114.584805.

748 Hayashi, S., Uehara, D.T., Tanimoto, K., Mizuno, S., Chinen, Y., Fukumura, S., Takanashi, J.I.,
749 Osaka, H., Okamoto, N., and Inazawa, J. (2017). Comprehensive investigation of CASK mutations
750 and other genetic etiologies in 41 patients with intellectual disability and microcephaly with pontine
751 and cerebellar hypoplasia (MICPCH). PLoS One *12*, e0181791. 10.1371/journal.pone.0181791.

752 He, X., Cooley, K., Chung, C.H., Dashti, N., and Tang, J. (2007). Apolipoprotein receptor 2 and X11
753 alpha/beta mediate apolipoprotein E-induced endocytosis of amyloid-beta precursor protein and
754 beta-secretase, leading to amyloid-beta production. J Neurosci *27*, 4052-4060.
755 10.1523/JNEUROSCI.3993-06.2007.

756 Hill, K., Li, Y., Bennett, M., McKay, M., Zhu, X., Shern, J., Torre, E., Lah, J.J., Levey, A.I., and Kahn,
757 R.A. (2003). Munc18 interacting proteins: ADP-ribosylation factor-dependent coat proteins that
758 regulate the traffic of beta-Alzheimer's precursor protein. J Biol Chem *278*, 36032-36040.
759 10.1074/jbc.M301632200.

760 Ho, A., Liu, X., and Sudhof, T.C. (2008). Deletion of Mint proteins decreases amyloid production in
761 transgenic mouse models of Alzheimer's disease. J Neurosci *28*, 14392-14400.
762 10.1523/JNEUROSCI.2481-08.2008.

763 Ho, A., Morishita, W., Hammer, R.E., Malenka, R.C., and Sudhof, T.C. (2003). A role for Mints in
764 transmitter release: Mint 1 knockout mice exhibit impaired GABAergic synaptic transmission. Proc
765 Natl Acad Sci U S A *100*, 1409-1414. 10.1073/pnas.252774899.

766 Ho, C.S., Marinescu, V., Steinhilb, M.L., Gaut, J.R., Turner, R.S., and Stuenkel, E.L. (2002a).
767 Synergistic Effects of Munc18a and X11 Proteins on Amyloid Precursor Protein Metabolism. Journal
768 of Biological Chemistry *277*, 27021-27028. 10.1074/jbc.M201823200.

769 Ho, C.S., Marinescu, V., Steinhilb, M.L., Gaut, J.R., Turner, R.S., and Stuenkel, E.L. (2002b).
770 Synergistic effects of Munc18a and X11 proteins on amyloid precursor protein metabolism. J Biol
771 Chem *277*, 27021-27028. 10.1074/jbc.M201823200.

772 Holehouse, A.S., Ahad, J., Das, R.K., and Pappu, R.V. (2015). CIDER: Classification of Intrinsically
773 Disordered Ensemble Regions. Biophys. J. *108*, 228a.

774 Hornak, V., Abel, R., Okur, A., Strockbine, B., Roitberg, A., and Simmerling, C. (2006). Comparison
775 of multiple Amber force fields and development of improved protein backbone parameters. Proteins
776 *65*, 712-725. 10.1002/prot.21123.

777 Hornbeck, P.V., Zhang, B., Murray, B., Kornhauser, J.M., Latham, V., and Skrzypek, E. (2015).
778 PhosphoSitePlus, 2014: mutations, PTMs and recalibrations. Nucleic Acids Res *43*, D512-520.
779 10.1093/nar/gku1267.

780 Hsueh, Y.P. (2009). Calcium/calmodulin-dependent serine protein kinase and mental retardation.
781 Ann Neurol *66*, 438-443. 10.1002/ana.21755.

782 Hu, S.H., Christie, M.P., Saez, N.J., Latham, C.F., Jarrott, R., Lua, L.H., Collins, B.M., and Martin,
783 J.L. (2011). Possible roles for Munc18-1 domain 3a and Syntaxin1 N-peptide and C-terminal anchor
784 in SNARE complex formation. Proc Natl Acad Sci U S A *108*, 1040-1045. 10.1073/pnas.0914906108.

785 Humphreys, I.R., Pei, J., Baek, M., Krishnakumar, A., Anishchenko, I., Ovchinnikov, S., Zhang, J.,
786 Ness, T.J., Banjade, S., Bagde, S.R., et al. (2021). Computed structures of core eukaryotic protein
787 complexes. Science *374*, eabm4805. 10.1126/science.abm4805.

788 Hung, A.Y., and Sheng, M. (2002). PDZ domains: structural modules for protein complex assembly.
789 J Biol Chem *277*, 5699-5702. 10.1074/jbc.R100065200.

790 Huttlin, E.L., Bruckner, R.J., Navarrete-Perea, J., Cannon, J.R., Baltier, K., Gebreab, F., Gygi, M.P.,
791 Thornock, A., Zarraga, G., Tam, S., et al. (2021). Dual proteome-scale networks reveal cell-specific
792 remodeling of the human interactome. Cell *184*, 3022-3040 e3028. 10.1016/j.cell.2021.04.011.

793 Jones, K.A., Eng, A.G., Raval, P., Srivastava, D.P., and Penzes, P. (2014). Scaffold protein
794 X11alpha interacts with kalirin-7 in dendrites and recruits it to Golgi outposts. J Biol Chem *289*,
795 35517-35529. 10.1074/jbc.M114.587709.

796 Jumper, J., Evans, R., Pritzel, A., Green, T., Figurnov, M., Ronneberger, O., Tunyasuvunakool, K.,
797 Bates, R., Zidek, A., Potapenko, A., et al. (2021). Highly accurate protein structure prediction with
798 AlphaFold. Nature *596*, 583-589. 10.1038/s41586-021-03819-2.

799 Kasula, R., Chai, Y.J., Bademosi, A.T., Harper, C.B., Gormal, R.S., Morrow, I.C., Hosy, E., Collins,
800 B.M., Choquet, D., Papadopulos, A., and Meunier, F.A. (2016). The Munc18-1 domain 3a hinge-
801 loop controls syntaxin-1A nanodomain assembly and engagement with the SNARE complex during
802 secretory vesicle priming. J Cell Biol *214*, 847-858. 10.1083/jcb.201508118.

803 Kawabe, H., Nakanishi, H., Asada, M., Fukuhara, A., Morimoto, K., Takeuchi, M., and Takai, Y.
804 (2001). Pilt, a novel peripheral membrane protein at tight junctions in epithelial cells. J Biol Chem
805 *276*, 48350-48355. 10.1074/jbc.M107335200.

806 Ko, J., and Lee, J. (2021). Can AlphaFold2 predict protein-peptide complex structures accurately?
807 bioRxiv, 2021.2007.2027.453972. 10.1101/2021.07.27.453972.

808 Kondo, M., Shiono, M., Itoh, G., Takei, N., Matsushima, T., Maeda, M., Taru, H., Hata, S., Yamamoto,
809 T., Saito, Y., and Suzuki, T. (2010). Increased amyloidogenic processing of transgenic human APP
810 in X11-like deficient mouse brain. Mol Neurodegener *5*, 35. 10.1186/1750-1326-5-35.

811 Kondo, Y., Hanai, A., Nakai, W., Katoh, Y., Nakayama, K., and Shin, H.W. (2012). ARF1 and ARF3
812 are required for the integrity of recycling endosomes and the recycling pathway. Cell Struct Funct
813 *37*, 141-154. 10.1247/csf.12015.

814 Kubala, M.H., Kovtun, O., Alexandrov, K., and Collins, B.M. (2010). Structural and thermodynamic
815 analysis of the GFP:GFP-nanobody complex. Protein Sci *19*, 2389-2401. 10.1002/pro.519.

LaConte, L.E.W., Chavan, V., DeLuca, S., Rubin, K., Malc, J., Berry, S., Gail Summers, C., and Mukherjee, K. (2019). An N-terminal heterozygous missense CASK mutation is associated with microcephaly and bilateral retinal dystrophy plus optic nerve atrophy. Am J Med Genet A *179*, 94-103. 10.1002/ajmg.a.60687.

Lanoue, V., Chai, Y.J., Brouillet, J.Z., Weckhuysen, S., Palmer, E.E., Collins, B.M., and Meunier, F.A. (2019). STXBP1 encephalopathy: Connecting neurodevelopmental disorders with alpha-synucleinopathies? Neurology *93*, 114-123. 10.1212/WNL.0000000000007786.

Lee, D.S., Tomita, S., Kirino, Y., and Suzuki, T. (2000). Regulation of X11L-dependent amyloid precursor protein metabolism by XB51, a novel X11L-binding protein. J Biol Chem *275*, 23134-23138. 10.1074/jbc.C000302200.

Lee, H.Y., Park, J.B., Jang, I.H., Chae, Y.C., Kim, J.H., Kim, I.S., Suh, P.G., and Ryu, S.H. (2004). Munc-18-1 inhibits phospholipase D activity by direct interaction in an epidermal growth factor-reversible manner. J Biol Chem *279*, 16339-16348. 10.1074/jbc.M310976200.

Lee, J.H., Lau, K.F., Perkinton, M.S., Standen, C.L., Shemilt, S.J., Mercken, L., Cooper, J.D., McLoughlin, D.M., and Miller, C.C. (2003). The neuronal adaptor protein X11alpha reduces Abeta levels in the brains of Alzheimer's APPswe Tg2576 transgenic mice. J Biol Chem *278*, 47025-47029. 10.1074/jbc.M300503200.

Lee, Y., Kim, B.S., Choi, S., Lee, E.Y., Park, S., Hwang, J., Kwon, Y., Hyun, J., Lee, C., Kim, J.F., et al. (2019). Makes caterpillars floppy-like effector-containing MARTX toxins require host ADP-ribosylation factor (ARF) proteins for systemic pathogenicity. Proc Natl Acad Sci U S A *116*, 18031-18040. 10.1073/pnas.1905095116.

Leonoudakis, D., Conti, L.R., Radeke, C.M., McGuire, L.M., and Vandenberg, C.A. (2004). A multiprotein trafficking complex composed of SAP97, CASK, Veli, and Mint1 is associated with inward rectifier Kir2 potassium channels. J Biol Chem *279*, 19051-19063. 10.1074/jbc.M400284200.

Li, P., Merrill, S.A., Jorgensen, E.M., and Shen, K. (2016). Two Clathrin Adaptor Protein Complexes Instruct Axon-Dendrite Polarity. Neuron *90*, 564-580. 10.1016/j.neuron.2016.04.020.

Li, W., Xing, Y., Wang, Y., Xu, T., Song, E., and Feng, W. (2023). A non-canonical target-binding site in Munc18-1 domain 3b for assembling the Mint1-Munc18-1-syntaxin-1 complex. Structure *31*, 68-77 e65. 10.1016/j.str.2022.11.002.

Lin, A.Y., Henry, S., Reissner, C., Neupert, C., Kenny, C., Missler, M., Beffert, U., and Ho, A. (2019). A rare autism-associated MINT2/APBA2 mutation disrupts neurexin trafficking and synaptic function. Sci Rep *9*, 6024. 10.1038/s41598-019-42635-7.

Long, J.F., Feng, W., Wang, R., Chan, L.N., Ip, F.C., Xia, J., Ip, N.Y., and Zhang, M. (2005). Autoinhibition of X11/Mint scaffold proteins revealed by the closed conformation of the PDZ tandem. Nat Struct Mol Biol *12*, 722-728. 10.1038/nsmb958.

M. Okamoto, T.C.S.d. (1997). Mints, Munc18-interacting proteins in synaptic vesicle exocytosis. J. Biol. Chem *272*.

Mardones, G.A., Burgos, P.V., Lin, Y., Kloer, D.P., Magadan, J.G., Hurley, J.H., and Bonifacino, J.S. (2013). Structural basis for the recognition of tyrosine-based sorting signals by the mu3A subunit of the AP-3 adaptor complex. J Biol Chem *288*, 9563-9571. 10.1074/jbc.M113.450775.

Martin, S., Tomatis, V.M., Papadopulos, A., Christie, M.P., Malintan, N.T., Gormal, R.S., Sugita, S., Martin, J.L., Collins, B.M., and Meunier, F.A. (2013). The Munc18-1 domain 3a loop is essential for neuroexocytosis but not for syntaxin-1A transport to the plasma membrane. J Cell Sci *126*, 2353-2360. 10.1242/jcs.126813.

Matos, M.F., Xu, Y., Dulubova, I., Otwinowski, Z., Richardson, J.M., Tomchick, D.R., Rizo, J., and Ho, A. (2012). Autoinhibition of Mint1 adaptor protein regulates amyloid precursor protein binding and processing. Proc Natl Acad Sci U S A *109*, 3802-3807. 10.1073/pnas.1119075109.

Maximov, A., Sudhof, T.C., and Bezprozvanny, I. (1999). Association of neuronal calcium channels with modular adaptor proteins. J Biol Chem *274*, 24453-24456. 10.1074/jbc.274.35.24453.

McLoughlin, D.M., Standen, C.L., Lau, K.F., Ackerley, S., Bartnikas, T.P., Gitlin, J.D., and Miller, C.C. (2001). The neuronal adaptor protein X11alpha interacts with the copper chaperone for SOD1 and regulates SOD1 activity. J Biol Chem *276*, 9303-9307. 10.1074/jbc.M010023200.

Minami, S.S., Sung, Y.M., Dumanis, S.B., Chi, S.H., Burns, M.P., Ann, E.J., Suzuki, T., Turner, R.S., Park, H.S., Pak, D.T., et al. (2010). The cytoplasmic adaptor protein X11alpha and extracellular matrix protein Reelin regulate ApoE receptor 2 trafficking and cell movement. FASEB J *24*, 58-69. 10.1096/fj.09-138123.

Mirdita, M., Schutze, K., Moriwaki, Y., Heo, L., Ovchinnikov, S., and Steinegger, M. (2022). ColabFold: making protein folding accessible to all. Nat Methods *19*, 679-682. 10.1038/s41592-022-01488-1.

Mirdita, M., Steinegger, M., and Soding, J. (2019). MMseqs2 desktop and local web server app for fast, interactive sequence searches. Bioinformatics *35*, 2856-2858. 10.1093/bioinformatics/bty1057.

Motodate, R., Saito, H., Sobu, Y., Hata, S., Saito, Y., Nakaya, T., and Suzuki, T. (2019). X11 and X11-like proteins regulate the level of extrasynaptic glutamate receptors. J Neurochem *148*, 480-498. 10.1111/jnc.14623.

Motodate, R., Saito, Y., Hata, S., and Suzuki, T. (2016). Expression and localization of X11 family proteins in neurons. Brain Res *1646*, 227-234. 10.1016/j.brainres.2016.05.054.

Nakai, W., Kondo, Y., Saitoh, A., Naito, T., Nakayama, K., and Shin, H.W. (2013). ARF1 and ARF4 regulate recycling endosomal morphology and retrograde transport from endosomes to the Golgi apparatus. Mol Biol Cell *24*, 2570-2581. 10.1091/mbc.E13-04-0197.

Newell-Litwa, K., Chintala, S., Jenkins, S., Pare, J.F., McGaha, L., Smith, Y., and Faundez, V. (2010). Hermansky-Pudlak protein complexes, AP-3 and BLOC-1, differentially regulate presynaptic composition in the striatum and hippocampus. J Neurosci *30*, 820-831. 10.1523/JNEUROSCI.3400-09.2010.

Nourry, C., Grant, S.G., and Borg, J.P. (2003). PDZ domain proteins: plug and play! Sci STKE *2003*, RE7. 10.1126/stke.2003.179.re7.

Okamoto, M., and Sudhof, T.C. (1997). Mints, Munc18-interacting proteins in synaptic vesicle exocytosis. J Biol Chem *272*, 31459-31464. 10.1074/jbc.272.50.31459.

Okamoto, M., and Sudhof, T.C. (1998). Mint 3: a ubiquitous mint isoform that does not bind to munc18-1 or -2. Eur J Cell Biol *77*, 161-165. 10.1016/S0171-9335(98)80103-9.

Oughtred, R., Rust, J., Chang, C., Breitkreutz, B.J., Stark, C., Willems, A., Boucher, L., Leung, G., Kolas, N., Zhang, F., et al. (2021). The BioGRID database: A comprehensive biomedical resource of curated protein, genetic, and chemical interactions. Protein Sci *30*, 187-200. 10.1002/pro.3978.

Park, J.H., Jung, M.S., Kim, Y.S., Song, W.J., and Chung, S.H. (2012). Phosphorylation of Munc18-1 by Dyrk1A regulates its interaction with Syntaxin 1 and X11alpha. J Neurochem *122*, 1081-1091. 10.1111/j.1471-4159.2012.07861.x.

Peleg, Y., Vincentelli, R., Collins, B.M., Chen, K.E., Livingstone, E.K., Weeratunga, S., Leneva, N., Guo, Q., Remans, K., Perez, K., et al. (2021). Community-Wide Experimental Evaluation of the PROSS Stability-Design Method. J Mol Biol *433*, 166964. 10.1016/j.jmb.2021.166964.

Penzes, P., Johnson, R.C., Sattler, R., Zhang, X., Huganir, R.L., Kambampati, V., Mains, R.E., Eipper, B.A., (2001). The neuronal Rho-GEF Kalirin-7 interacts with PDZ domain-containing proteins and regulates dendritic morphogenesis. Neuron *29*, 229–242.

Peycheva, V., Kamenarova, K., Ivanova, N., Stamatov, D., Avdjieva-Tzavella, D., Alexandrova, I., Zhelyazkova, S., Pacheva, I., Dimova, P., Ivanov, I., et al. (2018). Chromosomal microarray analysis of Bulgarian patients with epilepsy and intellectual disability. Gene *667*, 45-55. 10.1016/j.gene.2018.05.015.

Piluso, G., D'Amico, F., Saccone, V., Bismuto, E., Rotundo, I.L., Di Domenico, M., Aurino, S., Schwartz, C.E., Neri, G., and Nigro, V. (2009). A missense mutation in CASK causes FG syndrome in an Italian family. Am J Hum Genet *84*, 162-177. 10.1016/j.ajhg.2008.12.018.

Poetz, F., Corbo, J., Levdansky, Y., Spiegelhalter, A., Lindner, D., Magg, V., Lebedeva, S., Schweiggert, J., Schott, J., Valkov, E., and Stoecklin, G. (2021). RNF219 attenuates global mRNA decay through inhibition of CCR4-NOT complex-mediated deadenylation. Nature Communications *12*, 7175. 10.1038/s41467-021-27471-6.

Robert, X., and Gouet, P. (2014). Deciphering key features in protein structures with the new ENDscript server. Nucleic Acids Res *42*, W320-324. 10.1093/nar/gku316.

Rogelj, B., Mitchell, J.C., Miller, C.C., and McLoughlin, D.M. (2006). The X11/Mint family of adaptor proteins. Brain Res Rev *52*, 305-315. 10.1016/j.brainresrev.2006.04.005.

Saito, Y., Akiyama, M., Araki, Y., Sumioka, A., Shiono, M., Taru, H., Nakaya, T., Yamamoto, T., and Suzuki, T. (2011). Intracellular trafficking of the amyloid beta-protein precursor (APP) regulated by novel function of X11-like. PLoS One *6*, e22108. 10.1371/journal.pone.0022108.

Sakamoto, M., Sasaki, K., Sugie, A., Nitta, Y., Kimura, T., Gursoy, S., Cinleti, T., Iai, M., Sengoku, T., Ogata, K., et al. (2021). De novo ARF3 variants cause neurodevelopmental disorder with brain abnormality. Hum Mol Genet *31*, 69-81. 10.1093/hmg/ddab224.

Sakuma, M., Tanaka, E., Taru, H., Tomita, S., Gandy, S., Nairn, A.C., Nakaya, T., Yamamoto, T., and Suzuki, T. (2009). Phosphorylation of the amino-terminal region of X11L regulates its interaction with APP. J Neurochem *109*, 465-475. 10.1111/j.1471-4159.2009.05988.x.

Saluja, I., Paulson, H., Gupta, A., and Turner, R.S. (2009). X11alpha haploinsufficiency enhances Abeta amyloid deposition in Alzheimer's disease transgenic mice. Neurobiol Dis *36*, 162-168. 10.1016/j.nbd.2009.07.006.

Sanger, A., Hirst, J., Davies, A.K., and Robinson, M.S. (2019). Adaptor protein complexes and disease at a glance. J Cell Sci *132*. 10.1242/jcs.222992.

Sano, Y., Syuzo-Takabatake, A., Nakaya, T., Saito, Y., Tomita, S., Itohara, S., and Suzuki, T. (2006). Enhanced amyloidogenic metabolism of the amyloid beta-protein precursor in the X11L-deficient mouse brain. J Biol Chem *281*, 37853-37860. 10.1074/jbc.M609312200.

Seong, E., Wainer, B.H., Hughes, E.D., Saunders, T.L., Burmeister, M., and Faundez, V. (2005). Genetic analysis of the neuronal and ubiquitous AP-3 adaptor complexes reveals divergent functions in brain. Mol Biol Cell *16*, 128-140. 10.1091/mbc.e04-10-0892.

Shetty, A., Sytnyk, V., Leshchyns'ka, I., Puchkov, D., Haucke, V., and Schachner, M. (2013). The neural cell adhesion molecule promotes maturation of the presynaptic endocytotic machinery by

switching synaptic vesicle recycling from adaptor protein 3 (AP-3)- to AP-2-dependent mechanisms. J Neurosci *33*, 16828-16845. 10.1523/JNEUROSCI.2192-13.2013.

Sifri, C., Hoeg, L., Durocher, D., and Setiaputra, D. (2023). An AlphaFold2 map of the 53BP1 pathway identifies a direct SHLD3-RIF1 interaction critical for DNA repair activity. bioRxiv, 2023.2001.2012.523815. 10.1101/2023.01.12.523815.

Simonetti, B., Guo, Q., Gimenez-Andres, M., Chen, K.-E., Moody, E.R.R., Evans, A.J., Danson, C.M., Williams, T.A., Collins, B.M., and Cullen, P.J. (2021). Mechanistic basis for SNX27-Retromer coupling to ESCPE-1 in promoting endosomal cargo recycling. bioRxiv, 2021.2008.2028.457928. 10.1101/2021.08.28.457928.

Stafford, R.L., Ear, J., Knight, M.J., and Bowie, J.U. (2011). The molecular basis of the Caskin1 and Mint1 interaction with CASK. J Mol Biol *412*, 3-13. 10.1016/j.jmb.2011.07.005.

Stepien, K.P., Xu, J., Zhang, X., Bai, X.C., and Rizo, J. (2022). SNARE assembly enlightened by cryo-EM structures of a synaptobrevin-Munc18-1-syntaxin-1 complex. Sci Adv *8*, eabo5272. 10.1126/sciadv.abo5272.

Sullivan, S.E., Dillon, G.M., Sullivan, J.M., and Ho, A. (2014). Mint proteins are required for synaptic activity-dependent amyloid precursor protein (APP) trafficking and amyloid beta generation. J Biol Chem *289*, 15374-15383. 10.1074/jbc.M113.541003.

Tabuchi, K., Biederer, T., Butz, S., and Sudhof, T.C. (2002). CASK participates in alternative tripartite complexes in which Mint 1 competes for binding with caskin 1, a novel CASK-binding protein. J Neurosci *22*, 4264-4273. 20026421.

Tamaki, H., Sanda, M., Katsumata, O., Hara, Y., Fukaya, M., and Sakagami, H. (2012). Pilt is a coiled-coil domain-containing protein that localizes at the trans-Golgi complex and regulates its structure. FEBS Lett *586*, 3064-3070. 10.1016/j.febslet.2012.07.051.

Tomita, S., Fujita, T., Kirino, Y., and Suzuki, T. (2000). PDZ domain-dependent suppression of NF-kappaB/p65-induced Abeta42 production by a neuron-specific X11-like protein. J Biol Chem *275*, 13056-13060. 10.1074/jbc.c000019200.

Tomita, S., Ozaki, T., Taru, H., Oguchi, S., Takeda, S., Yagi, Y., Sakiyama, S., Kirino, Y., and Suzuki, T. (1999). Interaction of a neuron-specific protein containing PDZ domains with Alzheimer's amyloid precursor protein. J Biol Chem *274*, 2243-2254. 10.1074/jbc.274.4.2243.

Tsaban, T., Varga, J., Avraham, O., Ben-Aharon, Z., Khramushin, A., and Schueler-Furman, O. (2021). Harnessing protein folding neural networks for peptide-protein docking. bioRxiv, 2021.2008.2001.454656. 10.1101/2021.08.01.454656.

Verhage, M., and Sorensen, J.B. (2020). SNAREopathies: Diversity in Mechanisms and Symptoms. Neuron *107*, 22-37. 10.1016/j.neuron.2020.05.036.

Voglmaier, S.M., Kam, K., Yang, H., Fortin, D.L., Hua, Z., Nicoll, R.A., and Edwards, R.H. (2006). Distinct endocytic pathways control the rate and extent of synaptic vesicle protein recycling. Neuron *51*, 71-84. 10.1016/j.neuron.2006.05.027.

Wu, X., Cai, Q., Chen, Y., Zhu, S., Mi, J., Wang, J., and Zhang, M. (2020). Structural Basis for the High-Affinity Interaction between CASK and Mint1. Structure *28*, 664-673 e663. 10.1016/j.str.2020.04.001.

Xie, X., Yan, X., Wang, Z., Zhou, H., Diao, W., Zhou, W., Long, J., and Shen, Y. (2013). Open-closed motion of Mint2 regulates APP metabolism. J Mol Cell Biol *5*, 48-56. 10.1093/jmcb/mjs033.

986 Ye, F., Zeng, M., and Zhang, M. (2018). Mechanisms of MAGUK-mediated cellular junctional
987 complex organization. Curr Opin Struct Biol *48*, 6-15. 10.1016/j.sbi.2017.08.006.

988 Yu, D., Chojnowski, G., Rosenthal, M., and Kosinski, J. (2023). AlphaPulldown-a python package
989 for protein-protein interaction screens using AlphaFold-Multimer. Bioinformatics *39*.
990 10.1093/bioinformatics/btac749.

991 Zhang, Y., Wang, Y.G., Zhang, Q., Liu, X.J., Liu, X., Jiao, L., Zhu, W., Zhang, Z.H., Zhao, X.L., and
992 He, C. (2009). Interaction of Mint2 with TrkA is involved in regulation of nerve growth factor-induced
993 neurite outgrowth. J Biol Chem *284*, 12469-12479. 10.1074/jbc.M809214200.

994 Zhang, Z., Lee, C.H., Mandiyan, V., Borg, J.P., Margolis, B., Schlessinger, J., and Kuriyan, J. (1997).
995 Sequence-specific recognition of the internalization motif of the Alzheimer's amyloid precursor
996 protein by the X11 PTB domain. EMBO J *16*, 6141-6150. 10.1093/emboj/16.20.6141.

997 Zhang, Z., Li, W., Yang, G., Lu, X., Qi, X., Wang, S., Cao, C., Zhang, P., Ren, J., Zhao, J., et al.
998 (2020). CASK modulates the assembly and function of the Mint1/Munc18-1 complex to regulate
999 insulin secretion. Cell Discov *6*, 92. 10.1038/s41421-020-00216-3.

1000

1001

1002

1003 **Figure legends**

1004 **Figure 1. The Mint1 MID interacts directly with Munc18-1 but not Munc18-3**

1005 **(A)** Schematic diagram of the human Mint proteins. (AHM, acidic α-heilcal motif; MID, Munc18-1-
1006 interacting domain; CID, CASK interacting domain; PTB, phosphotyrosine binding domain; PDZ1
1007 and PDZ2, Psd95/Dlg/ZO1 domains). **(B)** Pulldowns with GST-Mint1 MID show a direct interaction
1008 with purified Munc18-1 but not Munc18-3. Image shows Coomassie Blue stained gel. **(C)** Pulldowns
1009 with GST-tagged Mint1 truncated sequences identify residues 261-282 as sufficient and required for
1010 Munc18-1 binding. Image shows Coomassie Blue stained gel.

1011

1012 **Figure 2. A conserved sequence in Mint1 and Mint2 binds Munc18-1 and is not influenced by**
1013 **phosphorylation**

1014 **(A)** ITC of synthetic Mint1$^{261-282}$ peptide binding to purified Munc18-1. The top shows raw ITC data,
1015 and the bottom shows integrated and normalised data fit to a 1:1 binding model. **(B)** Sequences of
1016 peptides tested for Munc18-1 binding by ITC. The minimal and highly conserved sequence required
1017 for Munc18-1 binding is shaded. Mutated peptide residues are highlighted in blue. **(C)** Endogenous
1018 Munc18-1 is bound to GFP-tagged Mint1 but not the mutant GFP-Mint1$^{D269A/I270A}$. GFP-tagged Mint1
1019 proteins were transiently transfected into PC12 cells, immunoprecipitated with GFP-nanobody
1020 coupled beads, and the bound proteins probed by Western blot with anti-Munc18-1.

1021

1022 **Figure 3. Modelling of Munc18-1 in complex with the Mint1 AHM sequence.**

1023 **(A)** AlphaFold2 prediction of the complex between Munc18-1 and Mint1 AHM. The three top ranked
1024 models are overlaid and shown in backbone ribbon representation. The AHM is consistently
1025 modelled in an α-helical structure associated with the Munc18-1 domain3b (highlighted in blue). On
1026 the right the predicted alignment error (PAE) is plotted for each model. Signals in the off-diagonal
1027 regions indicate strong structural correlations between residues in the peptide with the Munc18-1
1028 protein. **Fig. S4** shows predictions of the full-length Munc18-1 and Mint1 complex as well as models
1029 of other Munc and Mint homologues and orthologues. (**B**) The top-ranked complex of Munc18-1 and
1030 the Mint1 AHM is shown in cartoon representation, with Munc18-1 domains highlighted. (**C**) As in (**B**)
1031 but the surface of Munc18-1 is shown coloured for sequence conservation as calculated by Consurf
1032 (Ashkenazy *et al.*, 2016). (**D**) Opposite views showing details of the Mint1 AHM bound to the
1033 Munc18-1 domain3b. (**E**) ITC of synthetic Mint1$^{261-282}$ peptide binding to purified Munc18-1 and
1034 structure-based mutants. The top shows raw ITC data, and the bottom shows integrated and
1035 normalised data fit to a 1:1 binding model. Mutated residues are highlighted in panel (**D**).

1036

1037 **Figure 4. Comparison of the predicted Munc18-1/Mint1 complex with experimental structures.**

1038 (**A**) Overlay of the Munc18-1 complex with Mint1 AHM predicted by AlphaFold2 and the recent crystal
1039 structure of the Munc18-1/Sx1a/Mint1 complex (Li *et al.*, 2023). The inset shows details of the
1040 binding site modelled by AlphaFold2 and observed in the crystal structure. The two structures are

identical in all key respects. (**B**) Overlay of the Munc18-1 complex with Mint1 AHM predicted by AlphaFold2 and the cryoEM structure of the Munc18-1/Sx1a/VAMP2 complex (Stepien *et al.*, 2022). The Mint1 AHM is expected to bind Munc18-1 independently of the Sxa1 t-SNARE and VAMP2 v-SNARE proteins.

Figure 5. Mint1 and Sx1a show allosteric effects on binding to Munc18-1

(A) Pulldowns with GST-Mint1 MID show that Munc18-1 domain3a hinge loop is important for binding. As Mint1 does not contact domain3a this suggests an allosteric effect on the domain3b binding site. Image shows Coomassie stained gel. **(B)** ITC of synthetic Mint1$^{261-282}$ peptide binding to purified Munc18-1 (red) and Munc18-1$^{\Delta 317-333}$ (black) confirm the requirement of domain3a for Mint1 interaction. **(C)** Pulldowns with GST-Mint1 MID show that Mint1 can bind Munc18-1 both alone and in the presence of Sx1a. Image shows Coomassie stained gel. **(D)** Although Mint1 and Sx1a can bind Munc18 simultaneously, ITC of Mint1 Mint1$^{261-282}$ AHM peptide binding to Munc18-1 in the absence (red) and presence (black) of Sx1a shows a reduction in binding affinity and enthalpy. **(E)** ITC of Sx1a binding to Munc18-1 in the absence (black) and presence (red) of synthetic Mint1$^{261-282}$ peptide. Together this shows there is a subtle allosteric inhibition of Sxa1 binding to Munc18-1 in the presence of Mint1. **(F)** ITC of Sx1a binding to Munc18-1$^{\Delta 317-333}$ in the absence (black) and presence (red) of synthetic Mint1$^{261-282}$ peptide.

Figure 6. Interactions of the Mint PTB domains with canonical and non-canonical peptide motifs predicted by AlphaFold2

(**A**) Overlay of the top-ranked AlphaFold2 predicted structures of the Mint1 PTB domain (blue) in complex with various NPxY-related peptide motifs (green) shown in backbone ribbon representation. These sequences are predicted to bind the canonical binding groove of the PTB domain (with similar interactions predicted for Mint2 (not shown)). The right panel shows details of the different sequences derived from various Mint-interacting transmembrane proteins. (**B**) Overlay of the top-ranked AlphaFold2 predicted structures of the Mint1 and Mint2 PTB domains (blue) in complex with the APP NPxY motif (green) and the N-terminal peptide of TJAP1 (brown) shown in backbone ribbon representation. (**C**) The top-ranked complex of Mint1 PTB domain bound to APP and TJAP1 is shown in cartoon representation. The lower panel shows the surface of Mint1 coloured for sequence conservation as calculated by Consurf (Ashkenazy *et al.*, 2016). (**D**) Details of the Mint1 PTB domain interaction with the TJAP1 peptide.

Figure 7. Interactions of the Mint PTB domains with canonical and non-canonical peptide motifs predicted by AlphaFold2

(**A**) Overlay of the top-ranked AlphaFold2 predicted structures of the Mint1 and Mint2 tandem PDZ domains (blue) in complex with ARF3 and ARF4 (green) shown in backbone ribbon representation. The middle panel shows the Mint1 complex with ARF3 in ribbon representation, with the position of

1079 GTP and Mg^{2+} based on the previous crystal structure of active ARF3-GTP (Lee *et al.*, 2019). The
1080 right panel shows the same image but with Mint1 surface coloured for sequence conservation as
1081 calculated by Consurf (Ashkenazy *et al.*, 2016). (**B**) Overlay of the top-ranked AlphaFold2 predicted
1082 structures of the Mint1 and Mint2 tandem PDZ domains (blue) in complex with the C-terminal PDZbm
1083 of NRX1 (green) shown in backbone ribbon representation. The middle panel shows the Mint1
1084 complex with ARF3 in ribbon representation. The right panel inset shows the details of the NRX1
1085 interaction with Mint1 PDZ2 domain. (**C**) Overlay of the top three ranked AlphaFold2 predicted
1086 structures of the Mint1 YxxΦ motif (blue) in complex with the C-terminal MHD of the AP3 μ3A subunit
1087 (green) shown in backbone ribbon representation. The middle panel shows the Mint1 complex with
1088 μ3A in ribbon representation. The right panel inset shows the details of the Mint1 YxxΦ motif
1089 interaction with μ3A.
1090
1091 **Figure 8. Mint1 structural model and interactions.**
1092 (**A**) Structural model of Mint1 derived from AlphaFold2 (Ammann *et al.*, 2016). (**B**) Schematic
1093 summary of Mint1-mediated interactions, and speculative model suggesting that at the cell surface
1094 Mint1 may act to reduce the affinity of Munc18-1 for the auto-inhibited Sx1a, thus enhancing the
1095 ability of Sx1a to associate with VAMP2 and SNAP25 to form the trans-SNARE assembly required
1096 for vesicle fusion. The C-terminal domains of Mint1 in contrast are associated with other proteins
1097 containing NPxY and PDZbm sequences and ARF small GTPases that may enhance Mint1
1098 membrane recruitment and modulate transmembrane protein trafficking.
1099
1100
1101
1102
1103
1104
1105
1106
1107
1108
1109
1110

1111 **Supplementary Information**

1112 **Figure S1. Sequence alignment of Mint proteins. (Related to Fig. 1)**

1113 (**A**) Sequence alignment Mint1 and Mint2. Alignment was performed with Multalin (Corpet et al.,
1114 1999) and rendered with ESPript3.0 (Robert and Gouet, 2014). Hs, *Homo sapiens*. Xt, *Xenopus*
1115 *tropicalis*. Dr, *Danio rerio*. Ce, *Caenorhabditis elegans*. Dv, *Drosophila virilis*.

1116

1117 **Figure S2. ITC experiments of Munc18-1 binding to various Mint peptides. (Related to Fig. 2)**

1118 Example ITC experiments are shown for each of the Mint peptides binding to Munc18-1 as described
1119 in **Fig. 2B** and Table 1. (**A**) Mint 1_1 (261-282) (**B**) Mint 1_1a (273-282) (**C**) Mint 1_1b (261-272) (**D**)
1120 Mint 1_1c (266-282) (**E**) Mint 1_4 (263-282) (**F**) Mint 1_5 (265-282) (**G**) Mint 1_6 (267-282) (**H**) Mint
1121 1_7 (261-280) (**I**) Mint 1_9 (261-276) (**J**) Mint 1_11 DI /AA (261-282 (**K**) Mint 1-12 DQ /AA (261-282)
1122 (**L**) Mint 1_13 IV/AA(261-282) (**M**) Mint 1_14 AE/AA(261-282) (**N**) Mint 1_2 (257-286) (**O**) Mint 1_3
1123 phosphomimetic (261-282) (**P**) Mint 2_2 phosphomimetic (219-242).

1124

1125 **Figure S3. Post-translational modifications and sequence charge distribution of human Mint1**
1126 **and Mint2. (Related to Fig. 2)**

1127 (**A**) Sites of phosphorylation and ubiquitination of human Mint1 and Mint2 experimentally observed
1128 and reported in PhosphoSitePlus (Hornbeck *et al.*, 2015). **(B)** Phosphorylation sites in the human
1129 Mint1 and Mint2 N-terminal regions documented in PhosphoSitePlus (Hornbeck *et al.*, 2015).
1130 Phosphomimetic mutations in regions adjacent to the Munc18-1 binding sequence do not influence
1131 affinity (**Fig. 2B; Table 1**). (**C**) Plot of the charge distribution versus the sequence of Mint1 and Mint2
1132 shows that the N-terminal disordered sequences have a high net-positive charge. Plots were made
1133 with CIDER (Holehouse et al., 2015).

1134

1135 **Figure S4. AlphaFold2 modelling of Munc18 interactions with Mint1. (Related to Fig. 3)**

1136 (**A**) Overlaid top three ranked models of human Mint1 bound to Munc18-1 from ColabFold shown in
1137 backbone ribbon representation. Mint1 is consistently modelled to bind Munc18-1 domain 3b via a
1138 short acidic α-helical motif (AHM) within its unstructured N-terminal domain (highlighted in blue). On
1139 the right hand side the predicted alignment error (PAE) is plotted for each model. Signals in the off-
1140 diagonal regions indicate strong structural correlations between residues in the peptide with the
1141 Munc18-1 protein. (**B**) Overlaid top three ranked models of the zebrafish Mint1 AHM sequence
1142 bound to Munc18-1 predicted with ColabFold. Similar to the human structures, the AHM is
1143 consistently modelled in an α-helical structure associated with the Munc18-1 domain3b (highlighted
1144 in blue). (**C**) Overlaid top three ranked models of the human Mint2 AHM sequence bound to Munc18-
1145 1 predicted with ColabFold. (**D**) Overlaid top three ranked models of the human Mint1 AHM
1146 sequence modelled with the non-binding Munc18-3 homologue. The AHM is modelled at several
1147 random positions (highlighted in blue). The PAE plots do not show evidence of significant interactions
1148 between the two proteins. (**E**) The top scoring model of the human Mint1 AHM and CID sequences

bound to Munc18-1 and CASK using ColabFold. The AHM region is predicted in an identical binding site on Munc18-1 to the isolated peptide sequence (highlighted in blue). The CID sequence is predicted to bind to CASK in almost essentially the same conformation as the two previous crystal structures (Wu *et al.*, 2020; Zhang *et al.*, 2020).

Figure S5. AlphaFold2 modelling of Mint1 interactions with proteins identified in BioGRID. (Related to Fig. 5 and 6)

Proteins identified in BioGRID as putative interactors of Mint1 and showing reasonable binding in AlphaFold2 predictions. The left panels show the top three ranked structures overlaid in backbone ribbon representation. On the right hand side, the predicted alignment error (PAE) is plotted for each model. Signals in the off-diagonal regions indicate strong structural correlations between residues in the peptide with the Mint1 protein. These focused predictions were performed on specific Mint1 domains with the ligand regions initially identified in high-throughput predictions of the two full-length proteins.

Figure S6. AlphaFold2 modelling of Mint2 interactions with proteins identified in BioGRID. (Related to Fig. 5 and 6)

Proteins identified in BioGRID as putative interactors of Mint2 and showing reasonable binding in AlphaFold2 predictions. The left panels show the top three ranked structures overlaid in backbone ribbon representation. On the right hand side the predicted alignment error (PAE) is plotted for each model. Signals in the off-diagonal regions indicate strong structural correlations between residues in the peptide with the Mint2 protein. These focused predictions were performed on specific Mint2 domains with the ligand regions initially identified in high-throughput predictions of the two full-length proteins.

1173 **Table 1: Thermodynamic parameters of Munc18-1 binding to Mint1 by ITC.**

1174

Syringe Sample	Peptide residues	Peptide sequences	K_d (μM)	N	Δ*H* (kcal/mol)	-TΔ*S* (kcal/mol)	Δ*G* (kcal/mol)
Mint1_1	261-282	MDSYEQEEDIDQIVAEVKQSMS	12.8	0.8	-9.51	2.84	-6.67
Mint1_1a	273-282	IVAEVKQSMS	-	/	/	/	/
Mint1_1b	261-272	MDSYEQEEDIDQ	-	/	/	/	/
Mint1_1c	266-282	QEEDIDQIVAEVKQSMS	21.	1	-1.16	-5.21	-6.38
Mint1_4	263-282	SYEQEEDIDQIVAEVKQSMS	12.9	1.3	-2.3	-4.38	-6.70
Mint1_5	265-282	EQEEDIDQIVAEVKQSMS	5.6	1.3	-3.48	-3.69	-7.17
Mint1_6	267-282	EEDIDQIVAEVKQSMS	4.0	1.2	-1.29	-6.08	-7.37
Mint1_7	261-280	MDSYEQEEDIDQIVAEVKQS	19.1	1	-1.78	-4.67	-6.44
Mint1_8	261-278	MDSYEQEEDIDQIVAEVK	-	/	/	/	/
Mint1_9	261-276	MDSYEQEEDIDQIVAE	-	/	/	/	/
Mint1_10	261-282 E267A/E268A	MDSYEQAADIDQIVAEVKQSMS	-	/	/	/	/
Mint1_11	261-282 D269A/I270A	MDSYEQEEAADQIVAEVKQSMS	-	/	/	/	/
Mint1_12	261-282 D271A/Q272A	MDSYEQEEDIAAIVAEVKQSMS	-	/	/	/	/
Mint1_13	261-282 I273A/V274A	MDSYEQEEDIDQAAAEVKQSMS	-	/	/	/	/
Mint1_14	261-282 A275A/E276A	MDSYEQEEDIDQIVAAVKQSMS	216	1.0	-57.6	52.6	-5.00
Mint1_2	257-286	PYPRMDSYEQEEDIDQIVAEVKQSMSSQSL	26.0	**1.3**	-4.21	-3.41	-7.62
Mint1_3	257-286 phosphomimic	PYPRMDEEEQEEDIDQIVAEVKQEMEEQEL	14.0	1.1	-6.5	-0.103	-6.60
Mint2_2	219-242 phosphomimic	LEDQEEDIDQIVAEIKMELEMEEI	200	1	-17.2	12.2	-5.05

1175

1176

1177 **Table 2: Thermodynamic parameters of Munc18-1 binding to Sx1a and Mint1(261-**
1178 **282) by ITC.**
1179

Syringe sample	Cell Sample	K_d (μM)	N	Δ*H* (kcal/mol)	-TΔ*S* (kcal/mol)	Δ*G* (kcal/mol)	Fold increase in K_d
Sx1a	Munc18-1	0.076	1	-20.6	9.53	-11.1	1
Sx1a +Mint1	Munc18-1 +Mint1	0.269	1	-29.7	20.7	-8.97	35
Mint1	Munc18-1	8.75	1	-7.90	0.918	-6.98	1
Mint1	Munc18-1 +Sx1a	20.6	1	-8.86	2.47	-6.40	2
Sx1a	Munc18-1$^{\Delta 317\text{-}333}$	0.11	1	-18.6	9.12	-9.48	1
Sx1a +Mint1	Munc18-1$^{\Delta 317\text{-}333}$ +Mint1	0.09	1	-18.8	9.17	-9.59	1

1180
1181

1182 **Resources Table.**

1183

REAGENT or RESOURCE	SOURCE or REFERENCE	IDENTIFIER
Bacterial Strains		
E. coli DH5α	Invitrogen	18265017
E. coli Rosetta™(DE3)	Merck Australia	70954
Cell Lines		
Pheochromocytoma cells (PC12)	ATCC	CRL-1721
Antibodies		
GFP polyclonal antibody	Thermo Fisher	A6455
BD Mouse Monoclonal anti-Munc18-1	BD Biosciences	610336
Goat anti mouse secondary antibody	Thermo Fisher	65-6120
Chemicals		
Benzamidine hydrochloride hydrate	Sigma Aldrich	B6506
Deoxyribonuclease I (DNase I)	Sigma Aldrich	DN25
Talon® resin	Clontech	635503
Glutathione Sepharose 4B	GE Healthcare	GEHE17-0756-0
Isopropyl β-D-1-thiogalactopyranoside	Bioline	Catalogue: BIO-37036
Recombinant DNA		
Plasmid: pGEX4T-2	Cytiva	28-9545-50
Plasmid: pGEX4T-2 GST- Mint1(226-314)(MID)	This study	N/A
Plasmid: pGEX4T-2 GST- Mint1(261-272)	This study	N/A
Plasmid: pGEX4T-2 GST- Mint1(261-282)	This study	N/A
Plasmid: pGEX4T-2 GST- Mint1(226-289)	This study	N/A
Plasmid: pGEX4T-2 GST- Mint1(222-314)	This study	N/A
Plasmid: pGEX4T-2 GST- Mint1(237-289)	This study	N/A
Plasmid: pcDNA3.1-N-eGFP Mint1-GFP	This study	N/A
Plasmid: pcDNA3.1-N-eGFP Mint1(D269A/I270A)-GFP	This study	N/A
Plasmid: pET24a(+) $Sx1a_{1-261}$-His	(Christie et al., 2012)	N/A
Plasmid: pET28a(+) Munc18-1-His	(Hu *et al.*, 2011)	N/A
Plasmid: pET28a(+) Munc18-$1^{\Delta 317-333}$-His	(Martin *et al.*, 2013)	N/A
pEGFP-N1	Clontec	6085-1
Deposited Data		
Minc18-1/Mint1/Sx1 complex (crystal structure)	RSCB Protein Data Bank	PDB ID: 7XSJ
Human Mint1 (protein sequence)	Uniprot	Q02410-1
Human Mint1 (open reading frame)	Genscript	NM_001163.3
Rat Munc18-1 (protein sequence)	Uniprot	P61765-1
Human Sx1a (protein sequence	Uniprot	Q16623-1
Human Mint1 interactome	BioGrid	https://thebiogrid.org/106817/summary/homo-sapiens/apba1.html
Human Mint2 interactome	BioGrid	https://thebiogrid.org/106818/summary/homo-sapiens/apba2.html

Software		
Pymol	Schrodinger, USA.	https://pymol.org/2/
BioGrid4.4.217	(Oughtred *et al.*, 2021)	https://thebiogrid.org
Consurf	(Ashkenazy *et al.*, 2016)	https://consurf.tau.ac.il/consurf_index.php
AlphaFold2 Multimer	(Evans *et al.*, 2022; Jumper *et al.*, 2021)	https://github.com/deepmind/alphafold
ColabFold and ColabFold batch	(Mirdita *et al.*, 2022)	https://github.com/sokrypton/ColabFold
Other		
Superose6 Increase10/300 GL	GE Healthcare	Catalogue: 29091596
HiLoad™ Superdex75 PG	GE Healthcare	Catalogue: 28989333

1186 **Table S1. Putative interactors of human Mint1 from BioGRID[a].**

1187

Uniprot Entry ID	Gene Names	AlphaFold predicted Interactor?[c]	Predicted interacting domains	References providing additional validation[b]
O14639	ABLIM1 ABLIM KIAA0059 LIMAB1	-		
Q15067	ACOX1 ACOX	-		
Q9Y2T2	AP3M1	+	C-terminal β-sandwich platform domain of AP3 μ3 subunit binds YxxΦ motif in Mint1	
P05067	APP A4 AD1	+	APP motif binds Mint1 PTB domain.	(Biederer *et al.*, 2002; Borg *et al.*, 1996; Matos *et al.*, 2012; Sakuma *et al.*, 2009; Xie *et al.*, 2013; Zhang *et al.*, 1997)
P61204	ARF3	+	ARF3 small GTPase binds Mint1 PDZ1-PDZ2 tandem domains.	(Hill *et al.*, 2003)
P18085	ARF4	-	ARF4 small GTPase binds Mint1 PDZ1-PDZ2 tandem domains.	(Hill *et al.*, 2003)
Q96DR7	ARHGEF26 SGEF HMFN1864	-		
Q9NXU5	ARL15 ARFRP2	-		
Q9UHR4	BAIAP2L1 IRTKS	-		
Q14012	CAMK1	-		
O14936	CASK LIN2	+	The CaM Kinase domain of CASK binds the CID motif of Mint1	(Borg *et al.*, 1998; Wu *et al.*, 2020; Zhang *et al.*, 2020)
O60563	CCNT1	-		
O14618	CCS	-		(McLoughlin et al., 2001)
Q12834	CDC20	-		
Q9P2B7	CFAP97 KIAA1430	-		
Q9Y6M4	CSNK1G3	-		
Q12959	DLG1	-		(Leonoudakis *et al.*, 2004)
P78352	DLG4 PSD95	-		
Q86SJ6	DSG4 CDHF13	-		
Q9H8V3	ECT2	-		
Q9H6Z9	EGLN3	-		
Q8TE02	ELP5 C17orf81 DERP6 HSPC002 MSTP071	-		
Q0PNE2	ELP6 ATP1 C3orf75 TMEM103	-		

P49841	GSK3B	-		
Q9NYZ3	GTSE1	-		
Q8WVV9	HNRNPLL HNRPLL SRRF BLOCK24	-		
P17482	HOXB9 HOX2E	-		
P31274	HOXC9 HOX3B	+	Homeobox domain of HOXC9 binds PTB domain of Mint1	
P28335	HTR2C HTR1C	-		(Becamel et al., 2002)
Q14500	KCNJ12 IRK2 KCNJN1	-	KCNJ12 motif binds Mint1 PTB domain.	(Leonoudakis *et al.*, 2004)
O60333	KIF1B KIAA0591 KIAA1448	-		
O00139	KIF2A KIF2 KNS2	-		
O95198	KLHL2	-		
Q6TFL4	KLHL24 DRE1	-		
Q9NS86	LANCL2 GPR69B TASP	-		
Q9UGP4	LIMD1	-		
O14910	LIN7A MALS1 VELI1	-		
Q9HAP6	LIN7B MALS2 VELI2 UNQ3116/PRO10200	-		(Leonoudakis *et al.*, 2004)
Q9NUP9	LIN7C MALS3 VELI3	-		(Leonoudakis *et al.*, 2004)
Q14114	LRP8 APOER2	+	LRP8 motif binds Mint2 PTB domain.	(He *et al.*, 2007)
Q9P0L2	MARK1 KIAA1477 MARK	-		
Q7L590	MCM10 PRO2249	-		
Q9BTE3	MCMBP C10orf119	-		
Q8WV92	MITD1	-		
P61764	Munc18-1 STXBP1 UNC18A	+	Munc18-1 domain3a binds Mint1 AHM.	(Biederer and Sudhof, 2000; Graham *et al.*, 2011; Han *et al.*, 2014; Ho *et al.*, 2002b; Li *et al.*, 2023; Okamoto and Sudhof, 1997; 1998; Park *et al.*, 2012). This study.
Q7Z628	NET1 ARHGEF8	-		
Q12986	NFX1 NFX2	-		
P52952	NKX2-5 CSX NKX2.5 NKX2E	-		
Q9BW91	NUDT9 NUDT10 PSEC0099 UNQ3012/PRO9771	-		
O95747	OXSR1 KIAA1101 OSR1	-		

Q6ZW49	PAXIP1 PAXIP1L PTIP CAGF28	-		
Q13526	PIN1	-		
Q99755	PIP5K1A	-		
Q99569	PKP4	-		
O00411	POLRMT	-		
Q13356	PPIL2	-		
Q9BZL6	PRKD2 PKD2 HSPC187	-		
P49810	PSEN2 AD4 PS2 PSNL2 STM2	-		(Biederer *et al.*, 2002)
Q5TGL8	PXDC1 C6orf145	-		
Q9NW64	RBM22 ZC3H16 199G4	-		
O94761	RECQL4 RECQ4	-		
Q8WVD3	RNF138 NARF HSD-4 HSD4	-		
Q96P16	RPRD1A P15RS	-		
P51812	RPS6KA3 ISPK1 MAPKAPK1B RSK2	-		
Q7L4I2	RSRC2	-		
P33764	S100A3 S100E	-		
Q86UD0	SAPCD2 C9orf140	-		
Q9BXP2	SLC12A9 CCC6 CIP1	-		
Q8N5C6	SRBD1	-		
Q8WVM0	TFB1M CGI-75	-		
Q5JTD0	TJAP1 PILT TJP4	-		
O95985	TOP3B TOP3B1	-		
Q9ULW0	TPX2 C20orf1 C20orf2 DIL2 HCA519	-		
Q8WVR3	TRAPPC14 C7orf43 MAP11	-		
Q9Y296	TRAPPC4 SBDN CGI-104 HSPC172 PTD009	-		
Q96Q05	TRAPPC9 KIAA1882 NIBP T1	-		
Q7Z2T5	TRMT1L C1orf25 TRM1L MSTP070	-		
Q9UPT9	USP22 KIAA1063 USP3L	+	USP domain of USP22 binds Mint1 PDZ1-PDZ2 tandem domains.	
Q8IWA0	WDR75 UTP17	-		
O95785	WIZ ZNF803	+	C-terminal Zinc-finger of WIZ binds the PDZ1-PDZ2 tandem domains of Mint1	
Q86U90	YRDC DRIP3 IRIP	-		
Q8N5A5	ZGPAT GPATC6 GPATCH6 KIAA1847 ZC3H9 ZC3HDC9 ZIP	-		

a. https://thebiogrid.org/106817/summary/homo-sapiens/apba1.html

1191 b. The BioGRID database provides references for each identified putative interaction. These are
1192 typically, although not always, high-throughput proteomics studies. Here we provide citations for
1193 other studies that have provided additional validation using methods such as immunoprecipitation,
1194 *in vitro* binding assays, or macromolecular structure determination.
1195
1196 c. The definition of “Interactor” is based on a semi-quantitative measure of the AlphaFold2-derived
1197 interfacial PTM (iPTM) score, visual inspection of the resultant PAE graphs and assessment of the
1198 structure in PyMOL. After generating single multimer predictions in AlphaFold2 in unsupervised
1199 batch mode, we found that a minimum iPTM score of 0.3 combined with a strong signal in the PAE
1200 plot for inter-molecular structural correlation provided a useful indicator for structural predictions for
1201 further assessment. In these cases, we then ran three independent modelling experiments to assess
1202 whether multiple predictions resulted in consistent structural alignments in PyMOL.
1203

1204 **Table S2. Putative interactors of human Mint2 from BioGRID[a].**

1205

Uniprot Entry ID	Gene Names	AlphaFold predicted Interactor?[c]	Predicted interacting domains	References providing additional validation[b]
Q6PD74	AAGAB	-		
Q9UBZ4	APEX2 APE2 APEXL2 XTH2	-		
P05067	APP A4 AD1	+	APP motif binds Mint2 PTB domain.	(Borg *et al.*, 1996; Matos *et al.*, 2012; Xie *et al.*, 2013; Zhang *et al.*, 1997)
P61204	ARF3	+	ARF3 small GTPase binds Mint2 PDZ1-PDZ2 tandem domains.	(Hill *et al.*, 2003)
P18085	ARF4	+	ARF4 small GTPase binds Mint2 PDZ1-PDZ2 tandem domains.	(Hill *et al.*, 2003)
Q7Z3C6	ATG9A APG9L1	-		
O15155	BET1	-		
Q9Y297	BTRC BTRCP FBW1A FBXW1A	-		
A6NLJ0	C2CD4B FAM148B NLF2	-		
O94985	CLSTN1 CS1 KIAA0911	+	CLSTN1 motif binds Mint2 PTB domain.	(Araki *et al.*, 2003)
Q9GZR7	DDX24	-		
Q09019	DMWD DM9	-		
Q9UKB1	FBXW11 BTRCP2 FBW1B FBXW1B KIAA0696	-		
A4D1S0	KLRG2 CLEC15B	-		
Q07954	LRP1 A2MR APR	+	LRP1 motif binds Mint2 PTB domain.	(Gotthardt *et al.*, 2000)
P98164	LRP2	+	LRP2 motif binds Mint2 PTB domain.	(Gotthardt *et al.*, 2000)
Q14114	LRP8 APOER2	+	LRP8 motif binds Mint2 PTB domain.	(Gotthardt *et al.*, 2000)
Q8N7X4	MAGEB6	-		
Q16659	MAPK6 ERK3 PRKM6	-		

P61764	Munc18-1 STXBP1 UNC18A	+	Munc18-1 domain3a binds Mint2 AHM.	(Biederer and Sudhof, 2000; Graham *et al.*, 2011; Han *et al.*, 2014; Ho *et al.*, 2002b; Li *et al.*, 2023; Okamoto and Sudhof, 1997; 1998; Park *et al.*, 2012). This study.
Q96P71	NECAB3 APBA2BP NIP1 SYTIP2 XB51	-		(Lee et al., 2000)
Q13393	PLD1	-		
P49810	PSEN2 AD4 PS2 PSNL2 STM2	-		(Biederer *et al.*, 2002)
O94761	RECQL4 RECQ4	-		
Q04206	RELA NFKB3	-		(Tomita et al., 2000)
Q9NVW2	RLIM RNF12	-		
Q68DV7	RNF43	-		
O15431	SLC31A1 COPT1 CTR1	-		
Q9HB58	SP110	-		
Q8N9I0	SYT2	-		
Q5JTD0	TJAP1 PILT TJP4	+	TJAP1 N-terminal sequence binds Mint2 PTB domain in non-canonical site	
Q8NFZ5	TNIP2 ABIN2 FLIP1	-		
Q8WV44	TRIM41 RINCK	-		
Q9Y2K6	USP20 KIAA1003 LSFR3A VDU2	-		
Q8TEY7	USP33 KIAA1097 VDU1	-		
Q6AHZ1	ZNF518A KIAA0335 ZNF518	-		

a. https://thebiogrid.org/106818/summary/homo-sapiens/apba2.html

b. The BioGRID database provides references for each identified putative interaction. These are typically, although not always, high-throughput proteomics studies. Here we provide citations for

other studies that have provided additional validation using methods such as immunoprecipitation, *in vitro* binding assays, or macromolecular structure determination.

c. The definition of “Interactor” is based on a semi-quantitative measure of the AlphaFold2-derived interfacial PTM (iPTM) score, visual inspection of the resultant PAE graphs and assessment of the structure in PyMOL. After generating single multimer predictions in AlphaFold2 in unsupervised batch mode, we found that a minimum iPTM score of 0.3 combined with a strong signal in the PAE plot for inter-molecular structural correlation provided a useful indicator for structural predictions for further assessment. In these cases, we then ran three independent modelling experiments to assess whether multiple predictions resulted in consistent structural alignments in PyMOL.

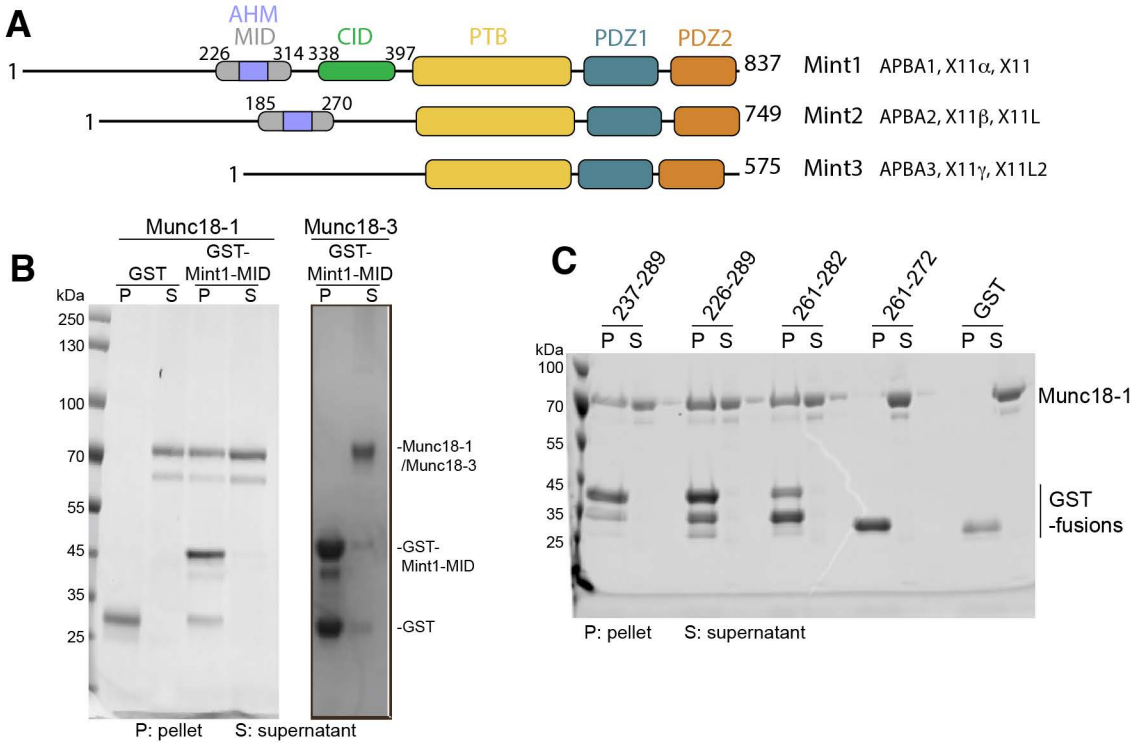

Figure 1. The Mint1 MID interacts directly with Munc18-1 but not Munc18-3
(A) Schematic diagram of the human Mint proteins. (AHM, acidic α-heilcal motif; MID, Munc18-1-interacting domain; CID, CASK interacting domain; PTB, phosphotyrosine binding domain; PDZ1 and PDZ2, Psd95/Dlg/ZO1 domains). (B) Pulldowns with GST-Mint1 MID show a direct interaction with purified Munc18-1 but not Munc18-3. Image shows Coomassie Blue stained gel. (C) Pulldowns with GST-tagged Mint1 truncated sequences identify residues 261-282 as sufficient and required for Munc18-1 binding. Image shows Coomassie Blue stained gel.

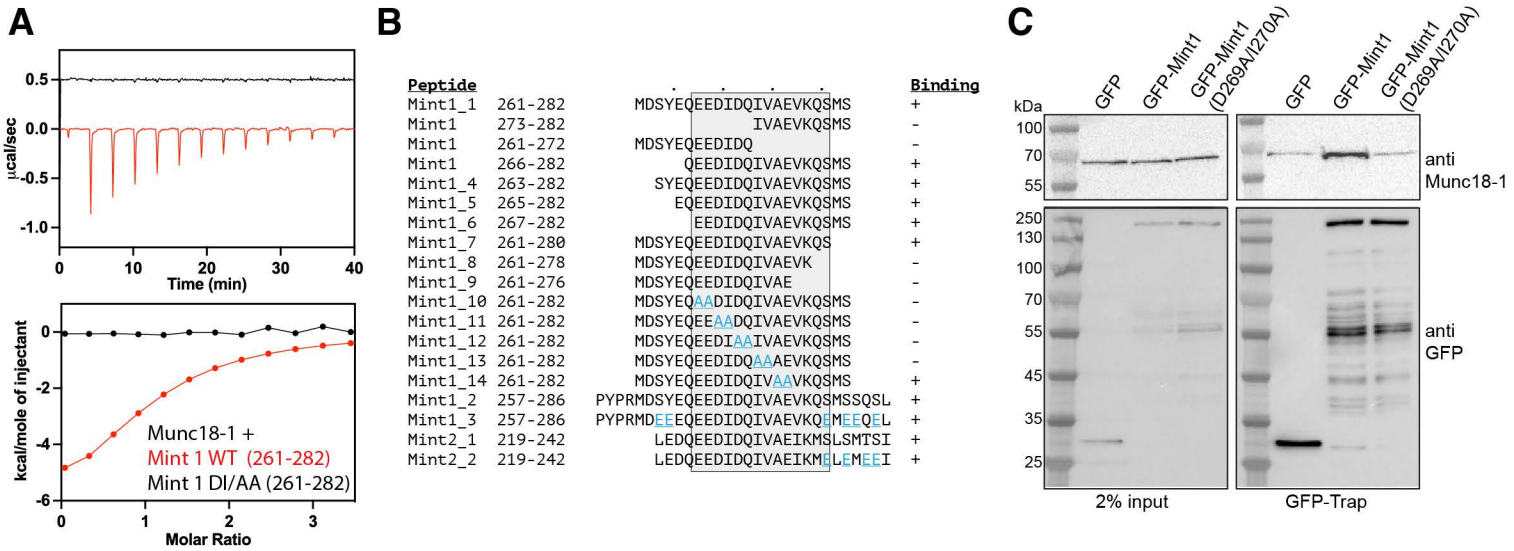

Figure 2. A conserved sequence in Mint1 and Mint2 binds Munc18-1 and is not influenced by phosphorylation
(A) ITC of synthetic Mint1261-282 peptide binding to purified Munc18-1. The top shows raw ITC data, and the bottom shows integrated and normalised data fit to a 1:1 binding model. (B) Sequences of peptides tested for Munc18-1 binding by ITC. The minimal and highly conserved sequence required for Munc18-1 binding is shaded. Mutated peptide residues are highlighted in blue. (C) Endogenous Munc18-1 is bound to GFP-tagged Mint1 but not the mutant GFP-Mint1D269A/I270A. GFP-tagged Mint1 proteins were transiently transfected into PC12 cells, immunoprecipitated with GFP-nanobody coupled beads, and the bound proteins probed by Western blot with anti-Munc18-1.

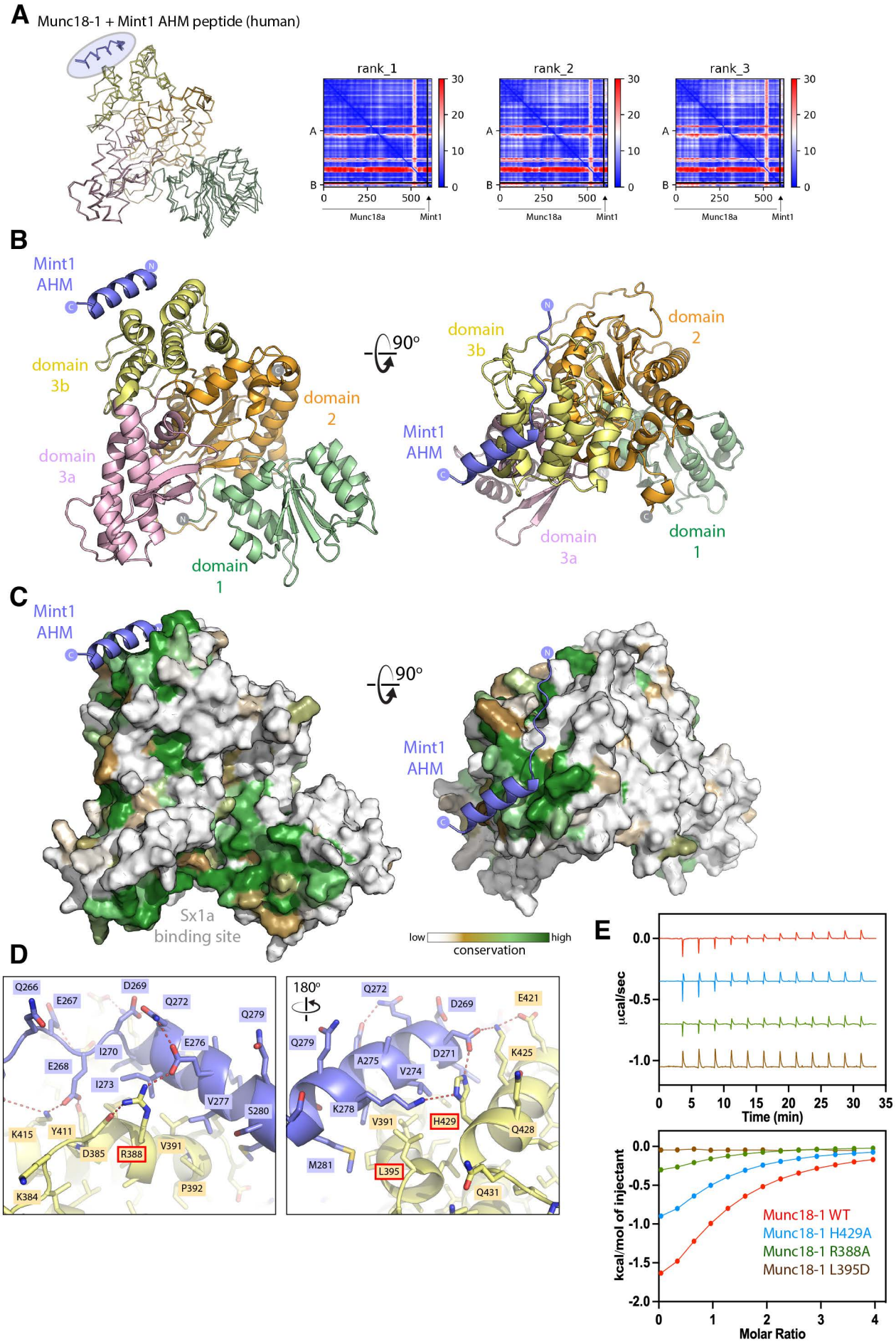

Figure 3. Modelling of Munc18-1 in complex with the Mint1 AHM sequence.
(A) AlphaFold2 prediction of the complex between Munc18-1 and Mint1 AHM. The three top ranked models are overlaid and shown in backbone ribbon representation. The AHM is consistently modelled in an α-helical structure associated with the Munc18-1 domain3b (highlighted in blue). On the right the predicted alignment error (PAE) is plotted for each model. Signals in the off-diagonal regions indicate strong structural correlations between residues in the peptide with the Munc18-1 protein. Fig. S4 shows predictions of the full-length Munc18-1 and Mint1 complex as well as models of other Munc and Mint homologues and orthologues. (B) The top-ranked complex of Munc18-1 and the Mint1 AHM is shown in cartoon representation, with Munc18-1 domains highlighted. (C) As in (B) but the surface of Munc18-1 is shown coloured for sequence conservation as calculated by Consurf (Ashkenazy et al., 2016). (D) Opposite views showing details of the Mint1 AHM bound to the Munc18-1 domain3b. (E) ITC of synthetic Mint1261-282 peptide binding to purified Munc18-1 and structure-based mutants. The top shows raw ITC data, and the bottom shows integrated and normalised data fit to a 1:1 binding model. Mutated residues are highlighted in panel (D).

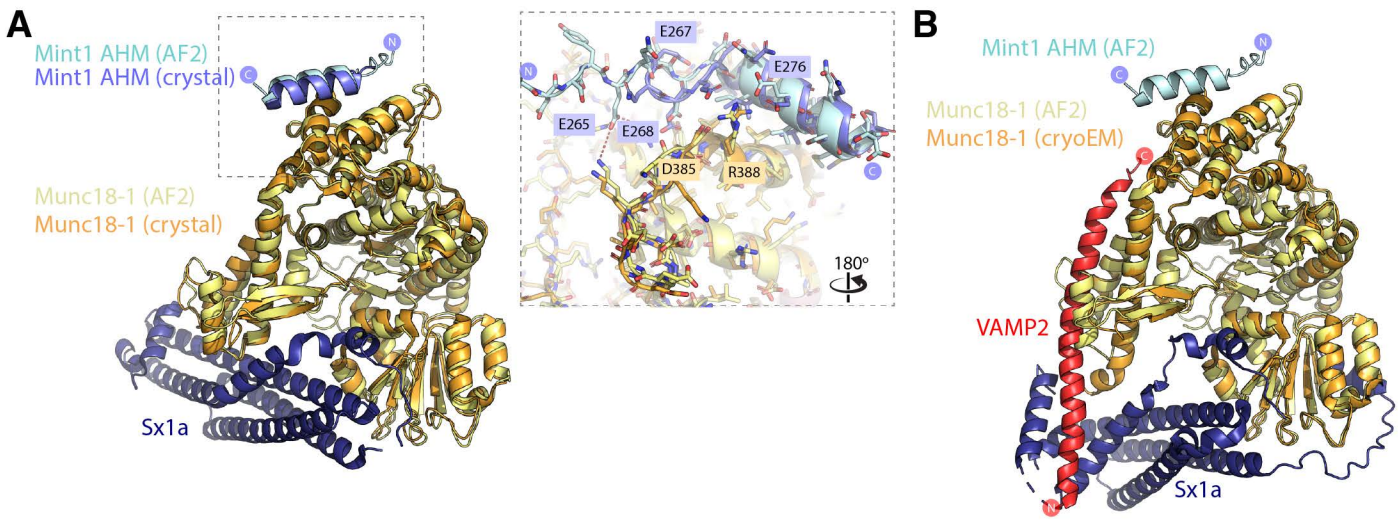

Figure 4. Comparison of the predicted Munc18-1/Mint1 complex with experimental structures.
(A) Overlay of the Munc18-1 complex with Mint1 AHM predicted by AlphaFold2 and the recent crystal structure of the Munc18-1/Sx-1a/Mint1 complex (Li et al., 2023). The inset shows details of the binding site modelled by AlphaFold2 and observed in the crystal structure. The two structures are identical in all key respects. (B) Overlay of the Munc18-1 complex with Mint1 AHM predicted by AlphaFold2 and the cryoEM structure of the Munc18-1/Sx1a/VAMP2 complex (Stepien et al., 2022). The Mint1 AHM is expected to bind Munc18-1 independently of the Sxa1 t-SNARE and VAMP2 v-SNARE proteins.

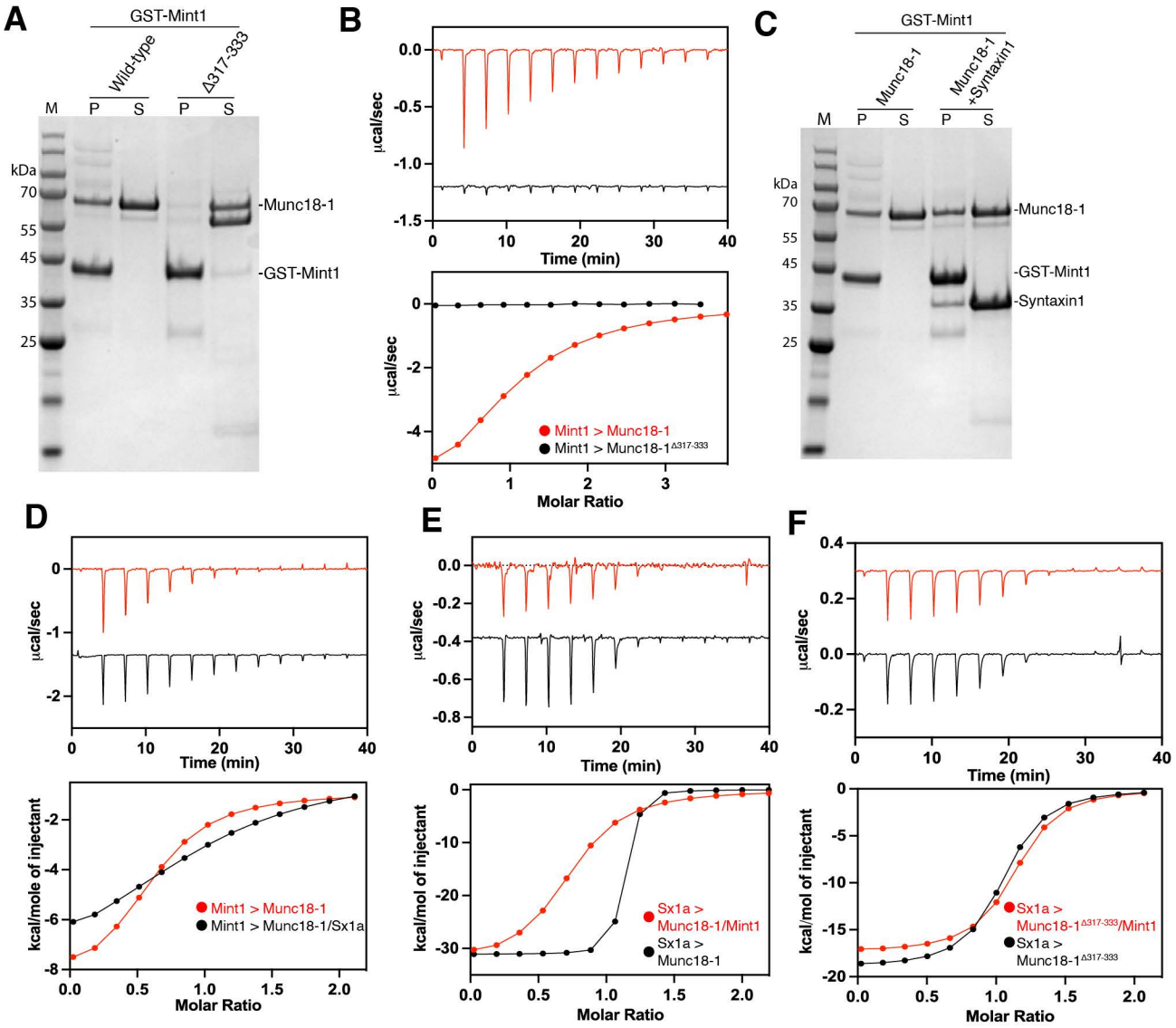

Figure 5. Mint1 and Sx1a show allosteric effects on binding to Munc18-1

(A) Pulldowns with GST-Mint1 MID show that Munc18-1 domain3a hinge loop is important for binding. As Mint1 does not contact domain3a this suggests an allosteric effect on the domain3b binding site. Image shows Coomassie stained gel. (B) ITC of synthetic Mint1261-282 peptide binding to purified Munc18-1 (red) and Munc18-1⊠317-333 (black) confirm the requirement of domain3a for Mint1 interaction. (C) Pulldowns with GST-Mint1 MID show that Mint1 can bind Munc18-1 both alone and in the presence of Sx1a. Image shows Coomassie stained gel. (D) Although Mint1 and Sx1a can bind Munc18 simultaneously, ITC of Mint1 Mint1261-282 AHM peptide binding to Munc18-1 in the absence (red) and presence (black) of Sx1a shows a reduction in binding affinity and enthalpy. (E) ITC of Sx1a binding to Munc18-1 in the absence (black) and presence (red) of synthetic Mint1261-282 peptide. Together this shows there is a subtle allosteric inhibition of Sxa1 binding to Munc18-1 in the presence of Mint1. (F) ITC of Sx1a binding to Munc18-1⊠317-333 in the absence (black) and presence (red) of synthetic Mint1261-282 peptide.

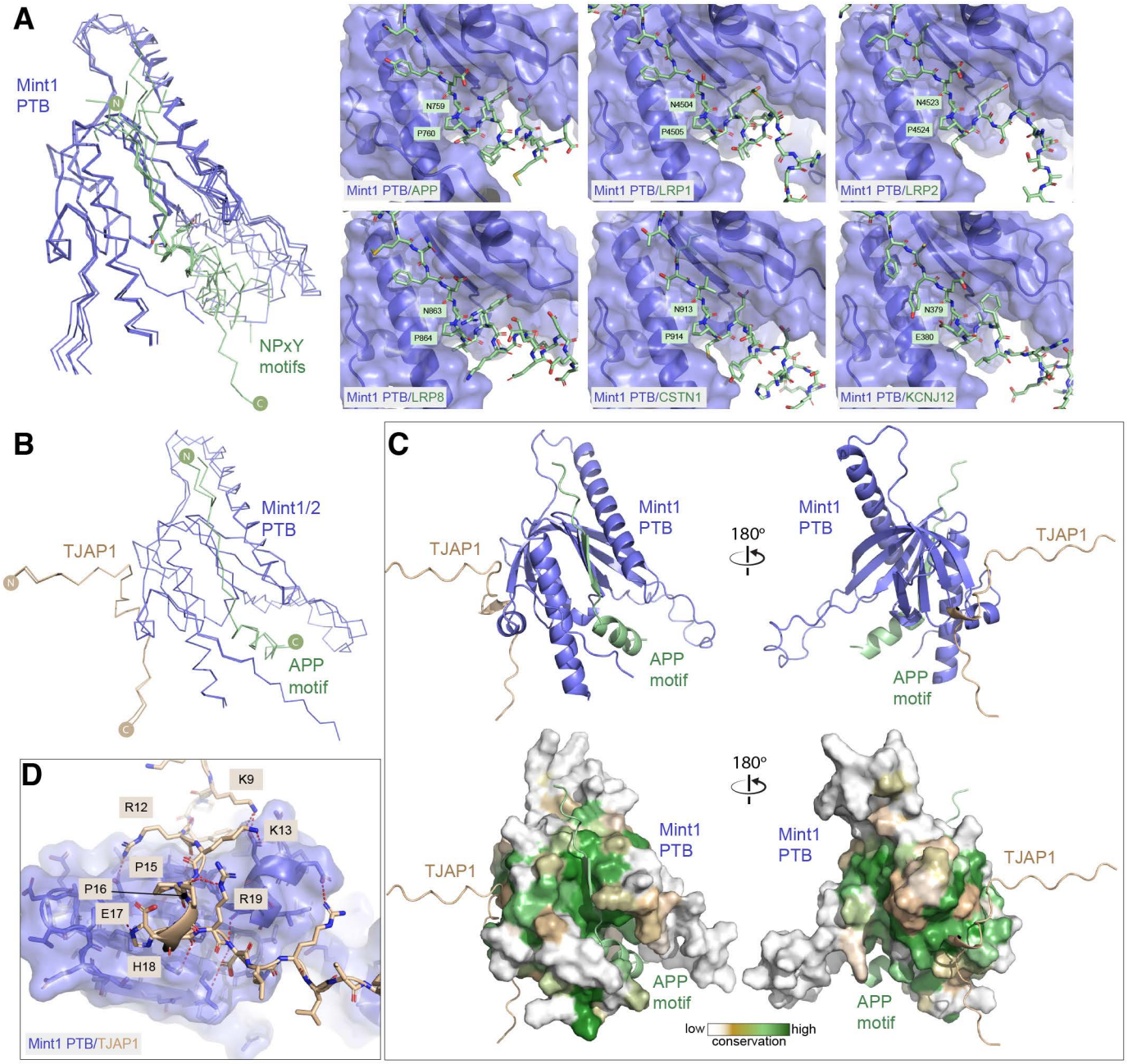

Figure 6. Interactions of the Mint PTB domains with canonical and non-canonical peptide motifs predicted by AlphaFold2
(A) Overlay of the top-ranked AlphaFold2 predicted structures of the Mint1 PTB domain (blue) in complex with various NPxY-related peptide motifs (green) shown in backbone ribbon representation. These sequences are predicted to bind the canonical binding groove of the PTB domain (with similar interactions predicted for Mint2 (not shown)). The right panel shows details of the different sequences derived from various Mint-interacting transmembrane proteins. (B) Overlay of the top-ranked AlphaFold2 predicted structures of the Mint1 and Mint2 PTB domains (blue) in complex with the APP NPxY motif (green) and the N-terminal peptide of TJAP1 (brown) shown in backbone ribbon representation. (C) The top-ranked complex of Mint1 PTB domain bound to APP and TJAP1 is shown in cartoon representation. The lower panel shows the surface of Mint1 coloured for sequence conservation as calculated by Consurf (Ashkenazy et al., 2016). (D) Details of the Mint1 PTB domain interaction with the TJAP1 peptide.

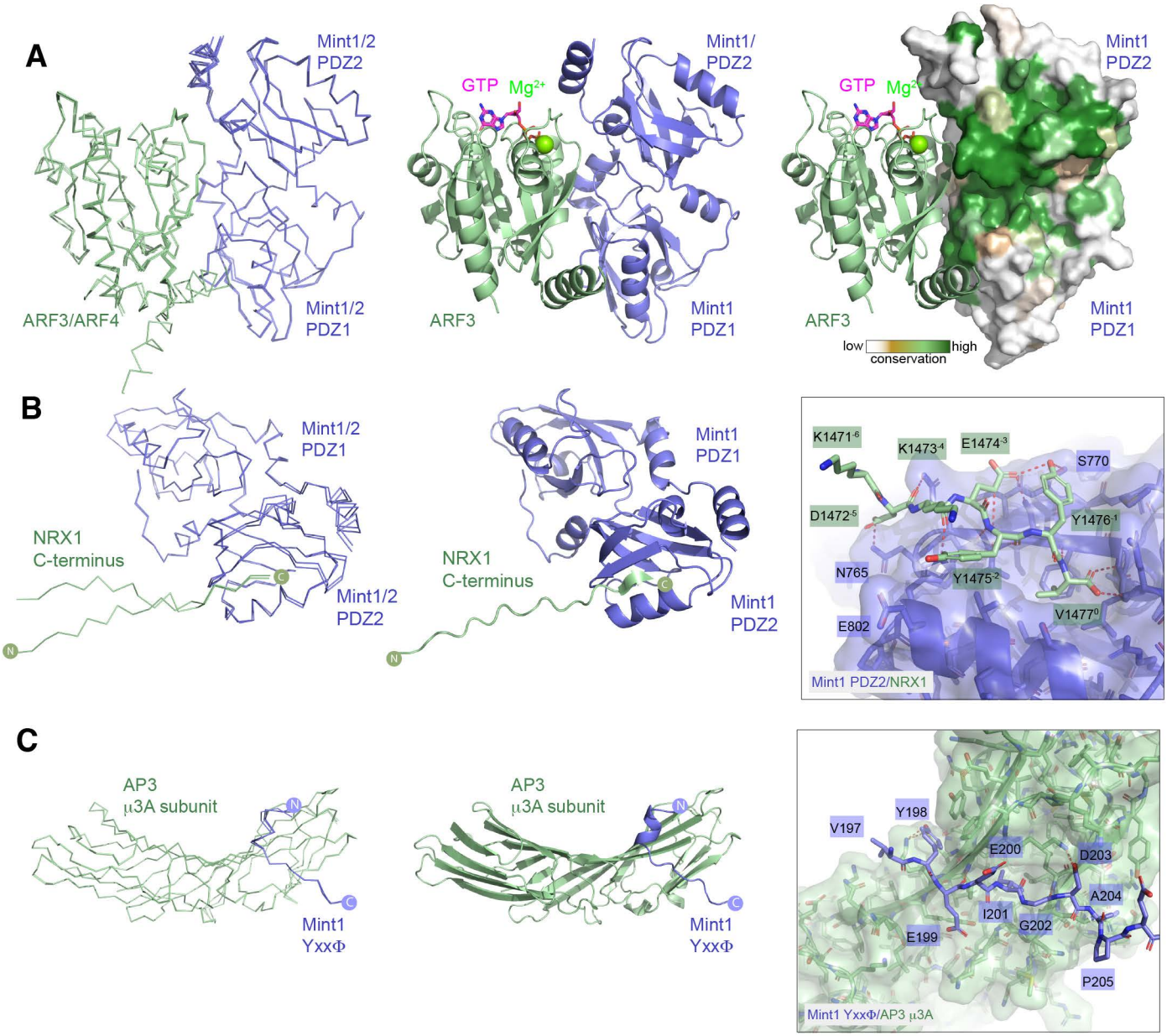

Figure 7. Interactions of the Mint PTB domains with canonical and non-canonical peptide motifs predicted by AlphaFold2
(A) Overlay of the top-ranked AlphaFold2 predicted structures of the Mint1 and Mint2 tandem PDZ domains (blue) in complex with ARF3 and ARF4 (green) shown in backbone ribbon representation. The middle panel shows the Mint1 complex with ARF3 in ribbon representation, with the position of GTP and Mg2+ based on the previous crystal structure of active ARF3-GTP (Lee et al., 2019). The right panel shows the same image but with Mint1 surface coloured for sequence conservation as calculated by Consurf (Ashkenazy et al., 2016). (B) Overlay of the top-ranked AlphaFold2 predicted structures of the Mint1 and Mint2 tandem PDZ domains (blue) in complex with the C-terminal PDZbm of NRX1 (green) shown in backbone ribbon representation. The middle panel shows the Mint1 complex with ARF3 in ribbon representation. The right panel inset shows the details of the NRX1 interaction with Mint1 PDZ2 domain. (C) Overlay of the top three ranked AlphaFold2 predicted structures of the Mint1 Yxx⊠ motif (blue) in complex with the C-terminal MHD of the AP3 ⊠3A subunit (green) shown in backbone ribbon representation. The middle panel shows the Mint1 complex with ⊠3A in ribbon representation. The right panel inset shows the details of the Mint1 Yxx⊠ motif interaction with ⊠3A.

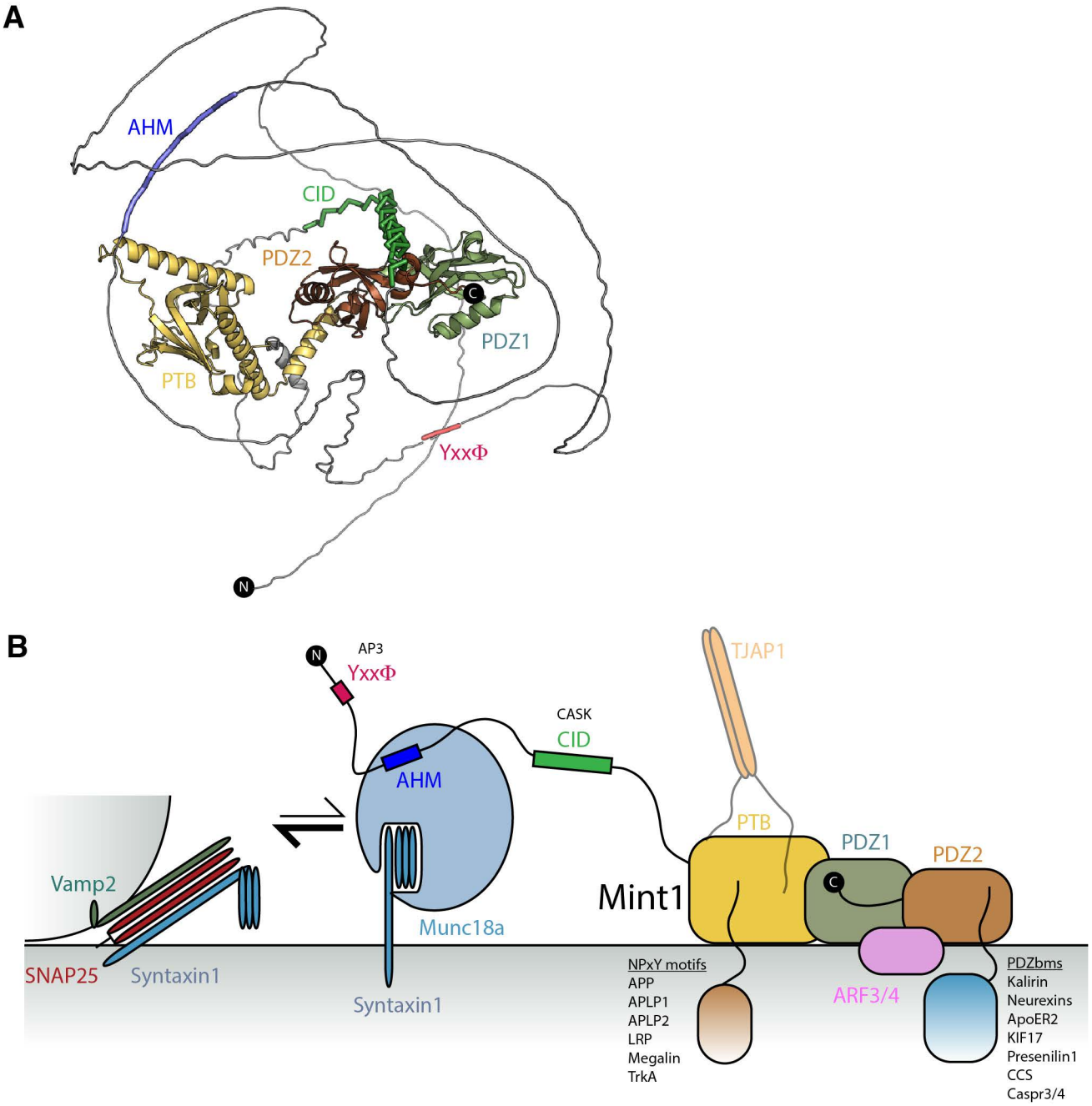

Figure 8. Mint1 structural model and interactions.
(A) Structural model of Mint1 derived from AlphaFold2 (Ammann et al., 2016). (B) Schematic summary of Mint1-mediated interactions, and speculative model suggesting that at the cell surface Mint1 may act to reduce the affinity of Munc18-1 for the auto-inhibited Sx1a, thus enhancing the ability of Sx1a to associate with VAMP2 and SNAP25 to form the trans-SNARE assembly required for vesicle fusion. The C-terminal domains of Mint1 in contrast are associated with other proteins containing NPxY and PDZbm sequences and ARF small GTPases that may enhance Mint1 membrane recruitment and modulate transmembrane protein trafficking.

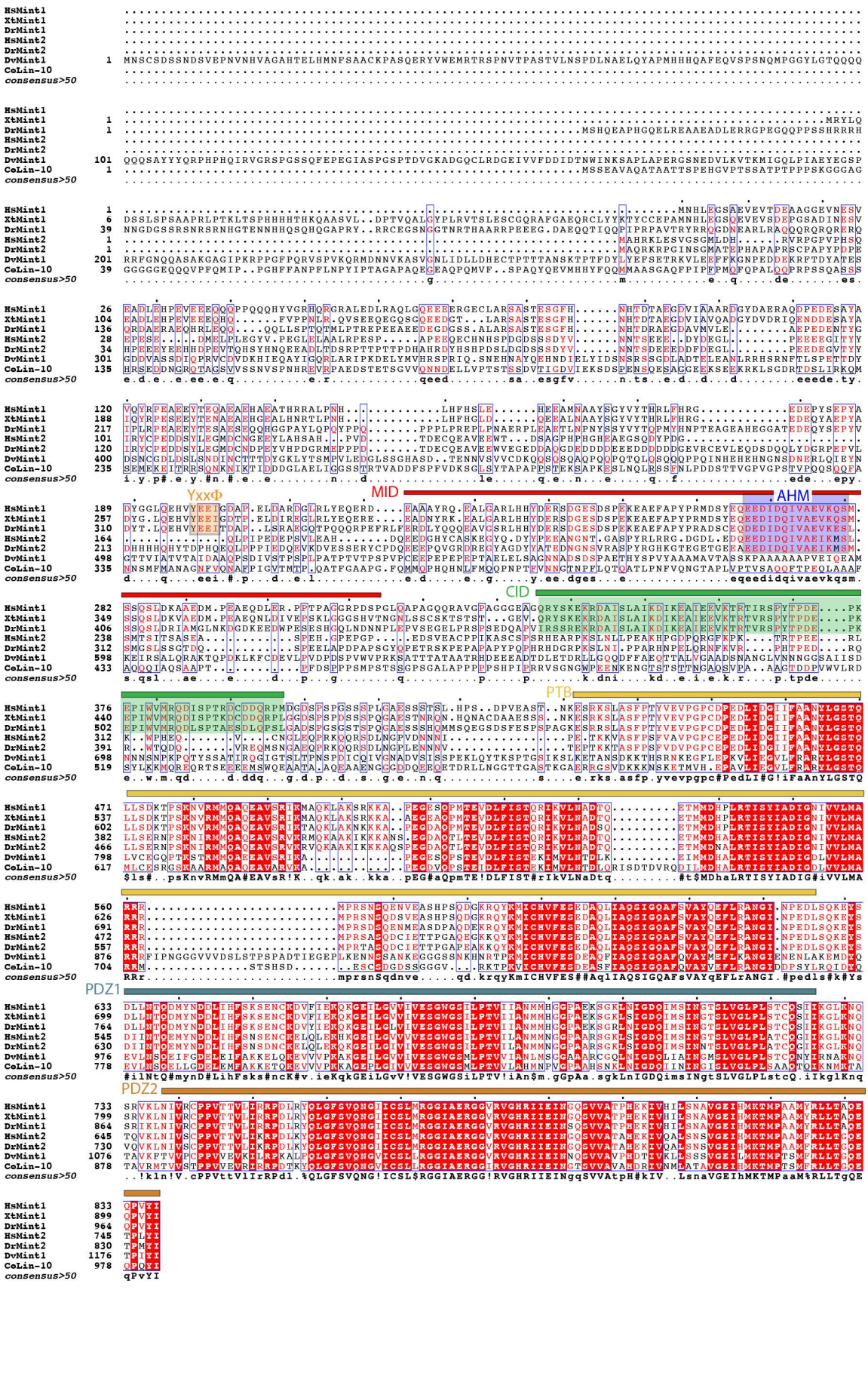

Figure S1. Sequence alignment of Mint proteins. (Related to Fig. 1)
(A) Sequence alignment Mint1 and Mint2. Alignment was performed with Multalin (Corpet et al., 1999) and rendered with ESPript3.0 (Robert and Gouet, 2014). Hs, Homo sapiens. Xt, Xenopus tropicalis. Dr, Danio rerio. Ce, Caenorhabditis elegans. Dv, Drosophila virilis.

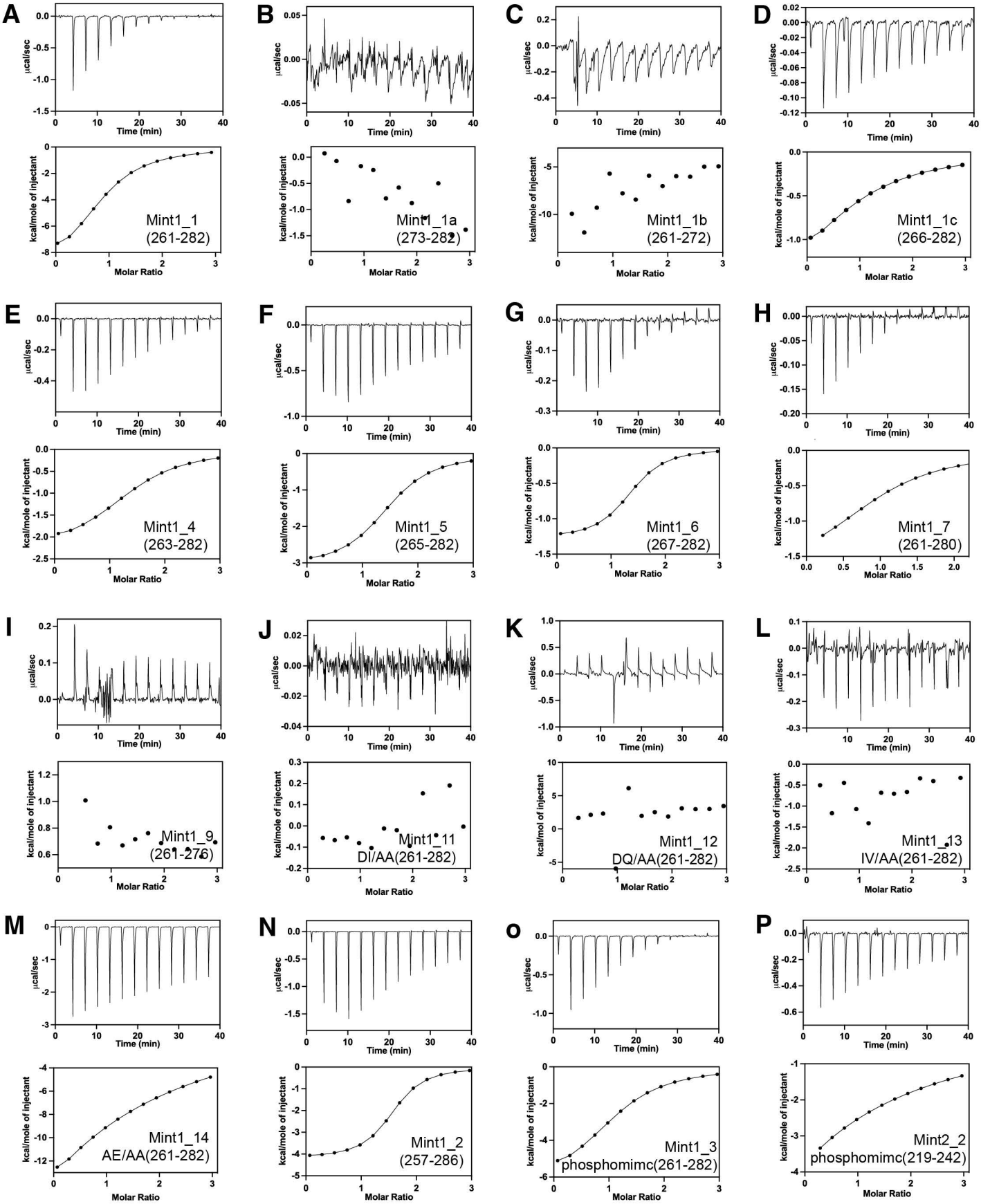

Figure S2. ITC experiments of Munc18-1 binding to various Mint peptides. (Related to Fig. 2)
Example ITC experiments are shown for each of the Mint peptides binding to Munc18-1 as described in Fig. 2B and Table 1. (A) Mint 1_1 (261-282) (B) Mint 1_1a (273-282) (C) Mint 1_1b (261-272) (D) Mint 1_1c (266-282) (E) Mint 1_4 (263-282) (F) Mint 1_5 (265-282) (G) Mint 1_6 (267-282) (H) Mint 1_7 (261-280) (I) Mint 1_9 (261-276) (J) Mint 1_11 DI /AA (261-282 (K) Mint 1-12 DQ /AA (261-282) (L) Mint 1_13 IV/AA(261-282) (M) Mint 1_14 AE/AA(261-282) (N) Mint 1_2 (257-286) (o) Mint 1_3 phosphomimetic (261-282) (P) Mint 2_2 phosphomimetic (219-242)

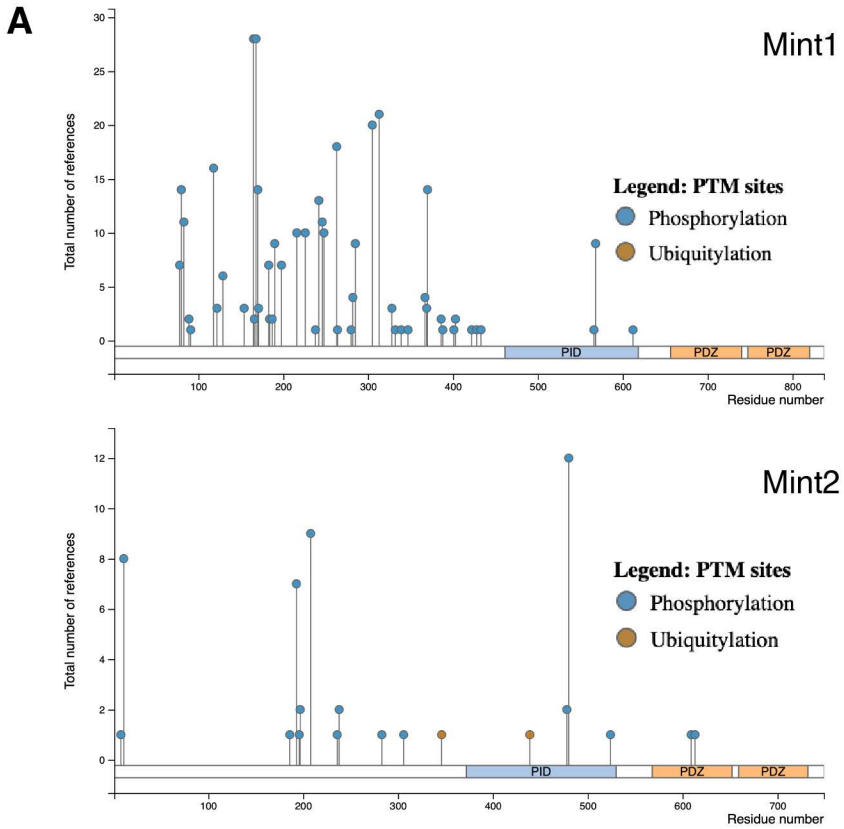

B

phosphorylation

```
hMint1  237-HYDERSDGESDSPEKEAEFAPYPRMDSYEQEEDIDQIVAEVKQSMSSQSLDKAAEDM
hMint2  193-YQDYYPEEANGNTGASPYRLRRGDGDLEDQEEDIDQIVAEIKMSLSMTSITSASEAS
                                          Munc18-binding
```

C

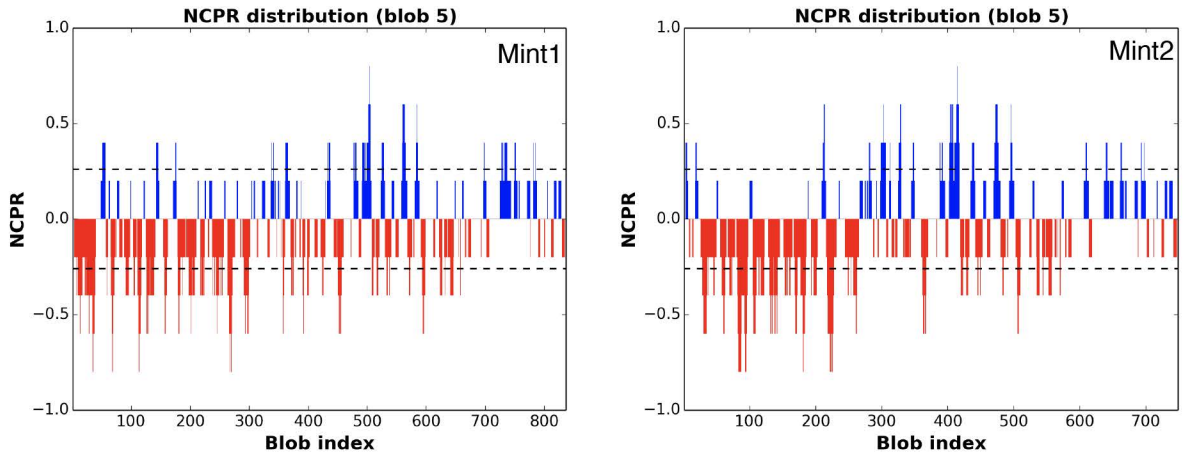

Figure S3. Post-translational modifications and sequence charge distribution of human Mint1 and Mint2. (Related to Fig. 2)
(A) Sites of phosphorylation and ubiquitination of human Mint1 and Mint2 experimentally observed and reported in PhosphoSitePlus (Hornbeck et al., 2015). (B) Phosphorylation sites in the human Mint1 and Mint2 N-terminal regions documented in PhosphoSitePlus (Hornbeck et al., 2015). Phosphomimetic mutations in regions adjacent to the Munc18-1 binding sequence do not influence affinity (Fig. 2B; Table 1). (C) Plot of the charge distribution versus the sequence of Mint1 and Mint2 shows that the N-terminal disordered sequences have a high net-positive charge. Plots were made with CIDER (Holehouse et al., 2015).

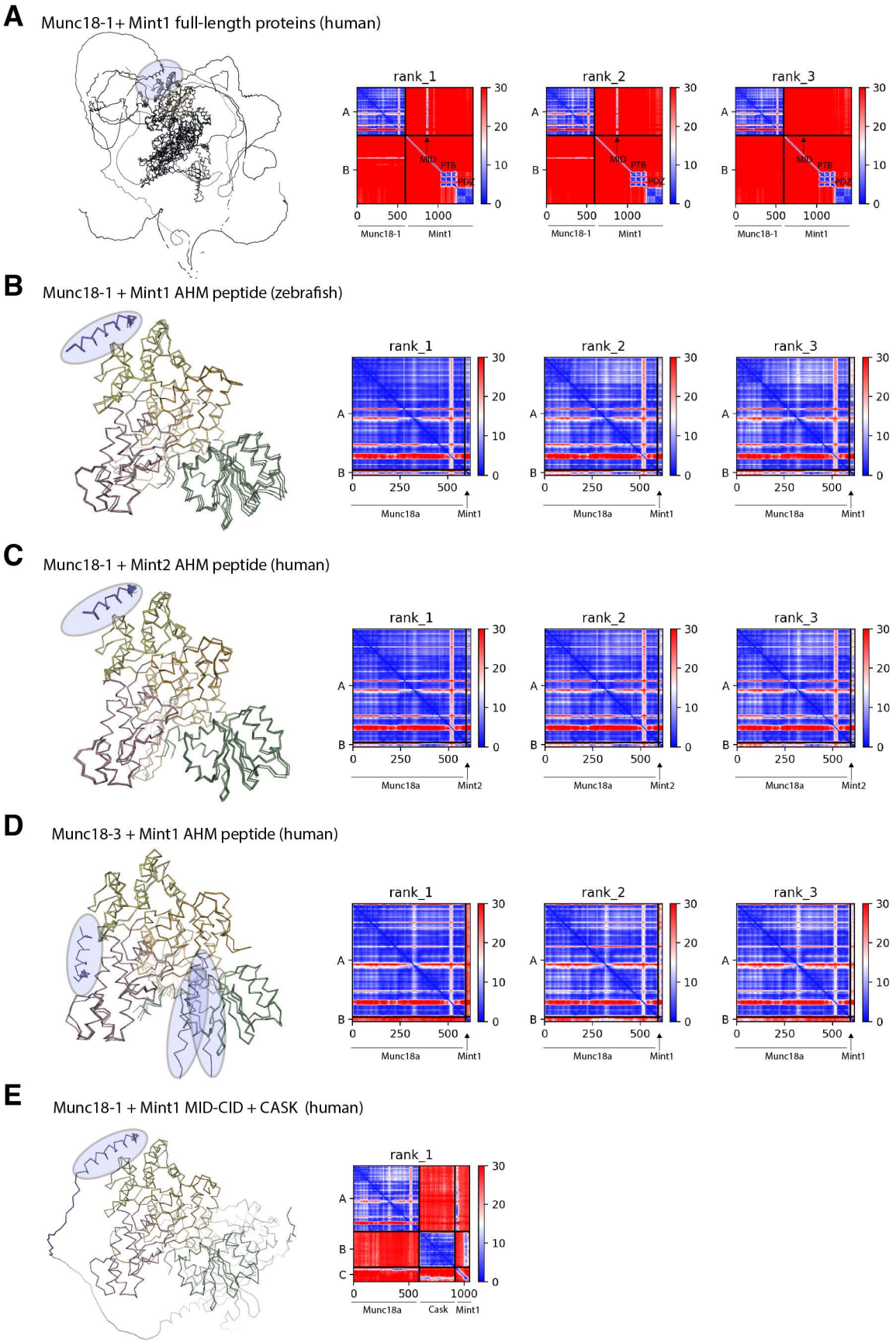

Figure S4. AlphaFold2 modelling of Munc18 interactions with Mint1. (Related to Fig. 3)
(A) Overlaid top three ranked models of human Mint1 bound to Munc18-1 from ColabFold shown in backbone ribbon representation. Mint1 is consistently modelled to bind Munc18-1 domain 3b via a short acidic α-helical motif (AHM) within its unstructured N-terminal domain (highlighted in blue). On the right hand side the predicted alignment error (PAE) is plotted for each model. Signals in the off-diagonal regions indicate strong structural correlations between residues in the peptide with the Munc18-1 protein. (B) Overlaid top three ranked models of the zebrafish Mint1 AHM sequence bound to Munc18-1 predicted with ColabFold. Similar to the human structures, the AHM is consistently modelled in an α-helical structure associated with the Munc18-1 domain3b (highlighted in blue). (C) Overlaid top three ranked models of the human Mint2 AHM sequence bound to Munc18-1 predicted with ColabFold. (D) Overlaid top three ranked models of the human Mint1 AHM sequence modelled with the non-binding Munc18-3 homologue. The AHM is modelled at several random positions (highlighted in blue). The PAE plots do not show evidence of significant interactions between the two proteins. (E) The top scoring model of the human Mint1 AHM and CID sequences bound to Munc18-1 and CASK using ColabFold. The AHM region is predicted in an identical binding site on Munc18-1 to the isolated peptide sequence (highlighted in blue). The CID sequence is predicted to bind to CASK in almost essentially the same conformation as the two previous crystal structures (Wu et al., 2020; Zhang et al., 2020).

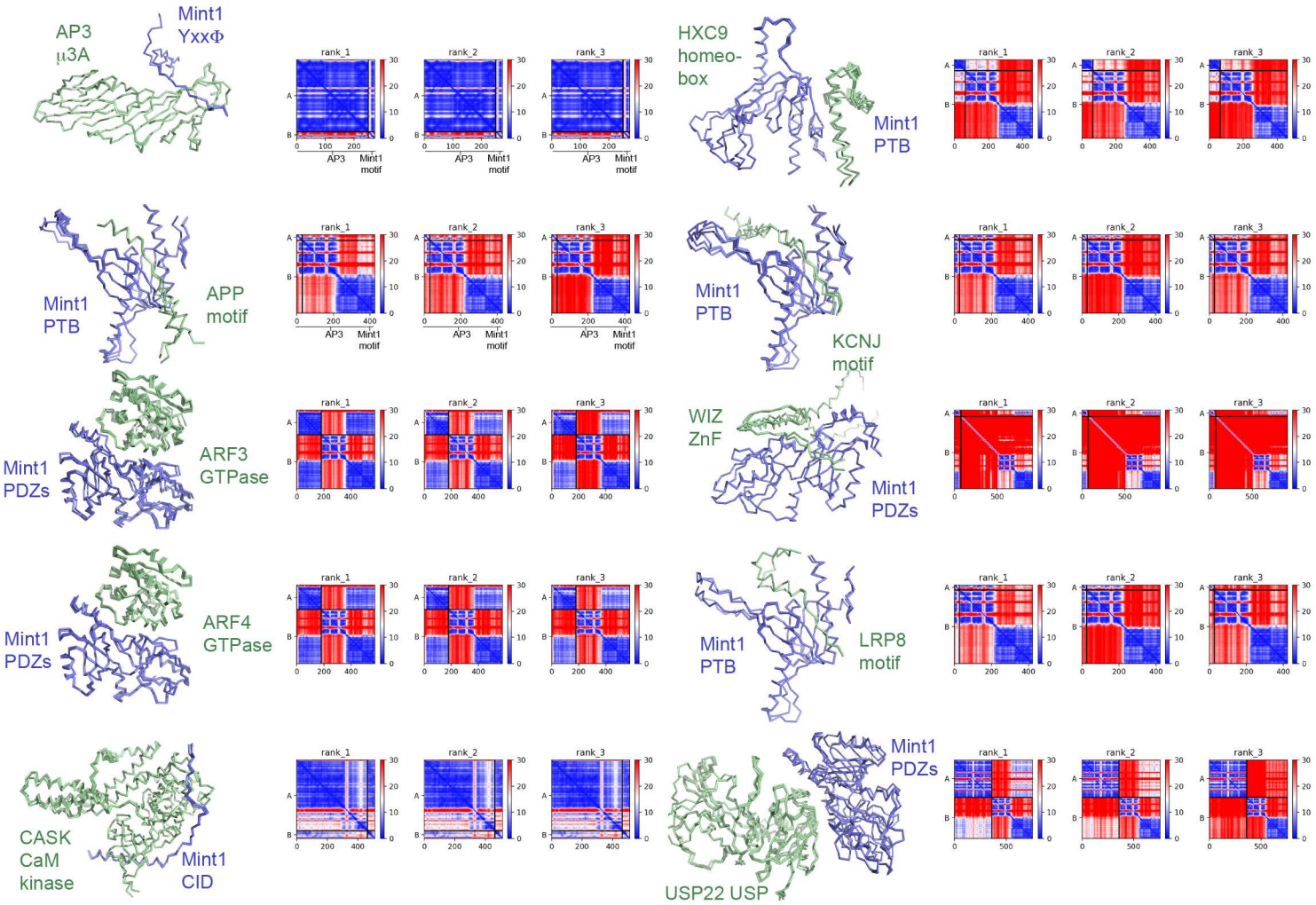

Figure S5. AlphaFold2 modelling of Mint1 interactions with proteins identified in BioGRID. (Related to Fig. 5 and 6)
Proteins identified in BioGRID as putative interactors of Mint1 and showing reasonable binding in AlphaFold2 predictions. The left panels show the top three ranked structures overlaid in backbone ribbon representation. On the right hand side the predicted alignment error (PAE) is plotted for each model. Signals in the off-diagonal regions indicate strong structural correlations between residues in the peptide with the Mint1 protein. These focused predictions were performed on specific Mint1 domains with the ligand regions initially identified in high-throughput predictions of the two full-length proteins.

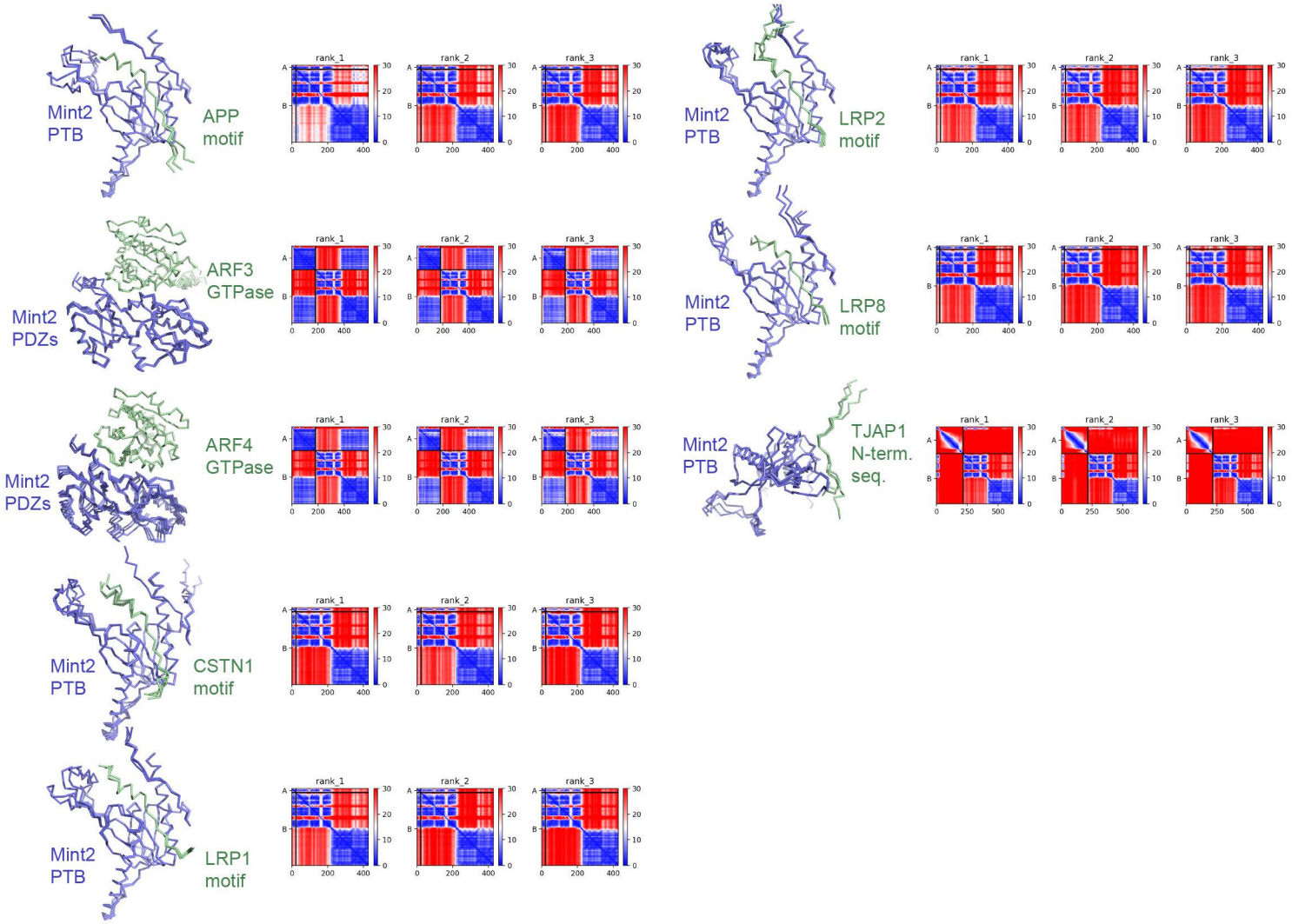

Figure S6. AlphaFold2 modelling of Mint2 interactions with proteins identified in BioGRID. (Related to Fig. 5 and 6)
Proteins identified in BioGRID as putative interactors of Mint2 and showing reasonable binding in AlphaFold2 predictions. The left panels show the top three ranked structures overlaid in backbone ribbon representation. On the right hand side the predicted alignment error (PAE) is plotted for each model. Signals in the off-diagonal regions indicate strong structural correlations between residues in the peptide with the Mint2 protein. These focused predictions were performed on specific Mint2 domains with the ligand regions initially identified in high-throughput predictions of the two full-length proteins.